

Low Z target optimization for spatial resolution improvement in planar imaging and cone-beam CT

Tanner Connell

Department of Medical Physics

McGill University, Montreal

June, 2009

*A thesis submitted to the Faculty of Graduate Studies and Research in partial fulfillment
of the requirements of the degree of Master of Science in Medical Radiation Physics*

© Tanner Connell 2009

ABSTRACT

Recent studies in medical physics have focused on the application of low atomic number (Z) targets for their effect on contrast in megavoltage portal imaging and cone-beam computed tomography (CBCT). This work seeks to compliment those studies by investigating the effects of varying different target parameters including atomic number, thickness and incident electron energy on spatial resolution in megavoltage planar imaging and CBCT. Target materials of beryllium (Be, Z = 4), aluminum (Al, Z = 13) and tungsten (W, Z = 74) were investigated over a variety thicknesses between 10% and 100% of the continuous slowing down approximation range. Incident electron kinetic energies of 4.5 MeV and 7.0 MeV were used along with custom targets installed into the carousel of a Varian 2100EX linear accelerator (Varian Medical, Inc.) to produce the experimental beams of interest. Monte Carlo simulated results were compared to measured data and it was shown that thinner targets are generally superior to thicker targets and that higher incident electron energies produce better results. Due to a dependence of the MTF of the detector system on photon energy, it was shown that low Z targets produced superior spatial resolution. Simulations also showed a 14.5% and 21.5% increase in spatial frequency in which the modulation transfer function dropped to half of its maximum (f_{50}) for the 7.0 MeV and 4.5 MeV targets, respectively, when moved from the carousel to the location of the clinical target. The f_{50} values of the custom targets were compared to the clinical 6 MV beam and were found to be between 10.4% lower and 15.5% higher than the 6 MV value. Low-Z CBCT sets were acquired using the CATphan phantom and compared to the clinical 6 MV beam and kilovoltage CBCT sets. Using the low-Z targets it was possible to resolve the 0.5 lp/mm, compared to 0.4 lp/mm and 1.0 lp/mm for the clinical 6 MV and kilovoltage sets respectively.

ABRÉGÉ

Récemment, plusieurs recherches se tournent vers l'emploi de cibles à petits numéros atomique (Z), et mesurent leurs effets sur le contraste de l'imagerie de portail de megavoltage et de tomographie calculée à faisceau cône (CBCT). À l'avenant, cet ouvrage étudie les effets de la variation de différents paramètres de la cible, tel le numéro atomique, l'épaisseur, et l'énergie de l'électron incident, sur la résolution spatiale des deux techniques d'imageries mentionnées. Des cibles de béryllium (Be, $Z = 4$), d'aluminium (Al, $Z = 13$), et de tungstène (W, $Z = 74$) sont étudiées sous une gamme d'épaisseurs entre 10 % et 100 % de l'amplitude de l'approximation de ralentissement continue (CSDA). Des électrons incidents avec des énergies cinétiques de 4.5 MeV et 7.0 MeV sont utilisés avec une cible personnalisée, installée sur le carrousel d'un accélérateur linéaire Varian 2100EX (Varian Medical, Inc.), afin de produire les faisceaux désirés. Des résultats Monte Carlo simulés sont comparés aux résultats mesurés. Les cibles minces sont généralement supérieures aux cibles plus épaisses, et les électrons incidents à plus haute énergie produisent de meilleurs résultats. Les cibles à petits Z produisent des résolutions supérieures en raison d'une dépendance du MTF du système de détection sur l'énergie des photons. Les simulations montrent une hausse de 14.5 % et de 21.5 % du f_{50} pour les cibles de 7.0 MeV et 4.5 MeV, respectivement, quand celles-ci sont déplacées du carrousel à l'emplacement clinique de la cible. Les f_{50} des cibles personnalisées sont entre 10.4 % sous et 15.5 % au-dessus du f_{50} du faisceau clinique à 6 MV. Les données pour le CBCT à petit Z sont obtenues avec un fantôme CATphan et comparées aux données du faisceau clinique à 6 MV et du CBCT de kilovoltage. Avec une cible à petit Z , une résolution de 0.5 lp/mm est atteinte, comparé à 0.4 lp/mm et 1.0 lp/mm pour le faisceau clinique à 6 MV et le CBCT de kilovoltage, respectivement.

ACKNOWLEDGMENTS

First and foremost, I would like to thank my project supervisor Dr. James Robar for all his support and encouragement over the past few years. His guidance and willingness to sit down at any time to discuss the many bumps along the road was much appreciated. Thank you James, it was a pleasure working together on this great project.

I would like to give special thanks to Dr. Ervin Podgorsak for giving me the opportunity to study at McGill. He has been a great inspiration and is an excellent teacher who I have learned a great deal from. I would also like to thank him for providing support and guidance in a difficult time.

I would also like to acknowledge the various faculty and staff at both the Medical Physics Unit and the Nova Scotia Cancer Center. Special thanks to all of my professors at McGill and the support staff at the NSCC (Ian, Scott, Ed and Rob). Thank you to Margery and Pam, two kind people who always seem to know the answers to my many questions.

Thank you to my fellow students and colleagues for their support. In particular I'd like to thank Guillaume, Claire, Mark and Arman for providing great friendship and always being there to provide help along the way during my time in Montreal and Alex for his help in talking through problems in my research in Halifax.

TABLE OF CONTENTS

Abstract.....	i
Abrégé.....	ii
Acknowledgements	iii
Table of contents	iv
List of tables	vii
List of figures.....	viii
Chapter 1: Introduction	1
1.1 Preface	1
1.2 Imaging as applied to radiotherapy.....	1
1.3 Previous work on improving image guidance in radiotherapy.....	2
1.4 Research goals.....	4
1.5 References	5
Chapter 2:Beam production and particle interactions	6
2.1 Introduction	6
2.2 Interactions of charged particles with matter.....	6
2.2.1 General aspects of Coulomb interactions.....	6
2.2.2 Stopping power.....	8
2.2.3 Range of charged particles	11
2.2.4 Production of x-rays.....	12
2.3 Photon interactions with matter	15
2.3.1 Compton scattering	15
2.3.2 Photoelectric effect	18
2.3.3 Pair production	20
2.4 Beam production in modern medical linear accelerators	22
2.5 References	26
Chapter 3: Radiation dosimeters and detection devices.....	26
3.1 Introduction.....	27

3.2	Film measurements.....	27
3.3	Electronic portal imaging devices.....	29
Chapter 4: Monte Carlo simulation of detection devices		31
4.1	Introduction	31
4.2	EGSnc and the BEAM code system.....	32
4.3	Improving efficiency in Monte Carlo simulations.....	34
4.4	References	36
Chapter 5: Materials and methods		37
5.1	Introduction	37
5.2	Low quality beam production	38
5.2.1	Choice of low-Z targets	38
5.2.2	Target placement and primary-electron filter.....	39
5.2.3	Operation of the accelerator in the experimental imaging mode ...	40
5.3	Experimental planar imaging	41
5.3.1	QC3 phantom.....	41
5.3.2	Image acquisition with the aS1000 electronic portal imager.....	42
5.3.3	Experimental image analysis.....	44
5.4	Monte Carlo model and simulations	46
5.4.1	Accelerator model.....	46
5.4.2	Model of spatial resolution phantom.....	48
5.4.3	Quantifying spatial resolution from generated phase spaces.....	49
5.4.4	Simulated investigation of photon focal spot size for various target combinations	50
5.5	Tracking the source of photons.....	52
5.5.1	Resolution improvement in moving the external target into the target arm.....	53
5.6	Spatial resolution assessment in cone-beam CT	53
5.6.1	Image acquisition, reconstruction and analysis.....	54
5.7	References	57
Chapter 6: Results and discussion		58
6.1	Introduction.....	58
6.2	Characterizing the incident electron beam.....	58
6.3	Tracking the source of photons.....	61
6.4	Simulation of focal spot size for various target parameter combinations	62
6.4.1	Simulation of electron beam broadening.....	64

6.4.2	Simulation of depth of photon creation	65
6.5	Simulated photon fluence from a modeled line pair phantom.....	66
6.6	Experimental determination of f50.....	68
6.7	Resolution improvement in moving the low-Z target into the target arm	72
6.8	Spatial resolution assessment in cone-beam CT	73
6.9	Clinical implementation of a low-Z, external target imaging mode	74
6.10	References.....	77
Chapter 7: Conclusion.....		78
7.1	Summary.....	78
7.2	Future Work	79
Bibliography		80
Appendix A: IAS3 parameters		83
Appendix B: Main BEAMnrc input file		84

LIST OF TABLES

Table 5.1: Actual thicknesses of the external targets in mm. .Error! Bookmark not defined.

Table 6.1: The percentage of photons created in different accelerator components that cross a $5 \times 5 \text{ cm}^2$ plane at isocenter.....Error! Bookmark not defined.

LIST OF FIGURES

Figure 2.1: The three different types of charged particle interactions with an atom. Hard, soft and radiative collisions are defined by the size of the impact parameter (b) relative to the atomic radius. 7

Figure 2.2: The mass collision (dashed lines) and mass radiative (solid lines) stopping power for electrons and positrons in three different materials. 11

Figure 2.3: The fluorescent yield for the k (ωk) and l (ωl) shells plotted against atomic number Z . The fraction of all photoelectric interactions that occur in the K shell PK for $h\nu > EBK$ and in the L shell PL for $h\nu > EBK$ 15

Figure 2.4: A schematic representation of a Compton interaction in which an incident photon scatters off of an orbital electron. 16

Figure 2.5: A representation of a pair production interaction in which an incident photon interacts with the Coulomb field of an atomic nucleus. Its energy is transferred into the creation of an electron-positron pair. 20

Figure 2.6: A block diagram of a modern medical linear accelerator ³ 23

Figure 3.1: A schematic representation of film layers. 28

Figure 3.2: A typical optical density curve as a function of exposure. 29

Figure 3.3: A schematic representation of the most common photon detection process in a modern electronic portal imaging device (EPID). The photon first passes into a metal plate and sets into motion an electron that interacts with a scintillator. Optical photons are emitted from the scintillator and are detected by a photodiode array. 30

Figure 5.1: (a) Installation of the custom targets into the carousel of the accelerator head. (b) The machined collar with an aluminum target and nylon sleeve used to hold the target at the correct position. 40

Figure 5.2: A block diagram illustrating the differences in the generation of the clinical 6 MV beam (left) and the experimental imaging beam (right). 41

Figure 5.3: The different contrast and spatial resolution regions of the QC3 phantom are shown..... 42

Figure 5.4: The experimental setup for planar imaging is shown, including the IDU20 panel, the imager base and the QC3 phantom..... 44

Figure 5.5: A typical fluence vs. position plot calculated from the phase using BEAMDP.	50
Figure 5.6: The experimental setup for cone-beam acquisition is shown including the CATphan phantom, stepping motor and digitization unit.	54
Figure 6.1: The digitized film regions at the upstream surface of the external target for the 4.5 MeV (a) and 7.0 MeV (b) incident electron beams respectively. (c) A typical dose profile across the film region exposed to the 4.5 MeV incident electron beam.	59
Figure 6.2: Electron fluence plotted as a function of radial position from the central axis for the 4.5 MeV and 7.0 MeV beams at the level of the external target. The electron fluence in vacuum is also shown for comparison.....	61
Figure 6.3: The photon focal spot half width at half maximum plotted as a function of $R_{\%CSDA}$ for various target parameters.	63
Figure 6.4: The electron fluence plotted as a function of radial position from the central axis is shown. The 7.0 MeV/Be and 7.0 MeV/W targets are shown for $R_{\%CSDA}$ values of 0%, 40% and 80%.	65
Figure 6.5: A relative frequency distribution of the depth in target of photon creation for the 4.5 MeV/Al, 7.0 MeV/Al, 7.0 MeV/W and 7.0 MeV/Be targets. 66	66
Figure 6.6: Simulated f_{50} values as a function of $R_{\%CSDA}$ for various target parameters. Included for comparison are the f_{50} values for the 4.5 MeV/Al and 7.0 MeV/Al targets at the location of the clinical target arm as well as the clinical 6 MV beam.	68
Figure 6.7: (a) A planar image of the QC3 taken with the clinical 6 MV beam. (b) The 20% thickness Be target with 7.0 MeV incident electrons which gave the highest f_{50} value. (c) The 100% thickness W target with 4.5 MeV incident electrons which gave the lowest f_{50} value.	71
Figure 6.8: Experimental f_{50} values for all target combinations as a function of target thickness as a percentage of R_{CSDA} . The f_{50} value from the clinical 6 MV beam is also included for comparison.	71
Figure 6.9: Monte Carlo generated relative fluence energy spectra for three custom targets, compared to the clinical 6 MV beam. Each curve is normalized by its area.....	72
Figure 6.10: MV CBCT axial slices of the spatial resolution section of the Catphan phantom acquired with the (a) 6 MV, (b) the 3.5 MeV/Al and the (c) 7.0 MeV/Al	

beams. (d) A cone beam set acquired of the same phantom using a 125 kVp
conventional simulator. **74**

Chapter 1

INTRODUCTION

1.1 PREFACE	1
1.2 IMAGING AS APPLIED TO RADIOTHERAPY.....	1
1.3 PREVIOUS WORK ON IMPROVING IMAGE GUIDANCE IN RADIOTHERAPY	2
1.4 RESEARCH GOALS	4
1.5 REFERENCES	5

1.1 Preface

X-Rays were accidentally discovered by Wilhelm Rontgen, a German physicist, in 1895 while performing routine experiments with a Crooks tube. This discovery soon led to the use of x rays for diagnostic purposes. By the 1920s, the damaging effects of radiation were known (first reported by Pierre Curie) and the potential applications of x-rays as a therapeutic tool was under investigation. Radium, discovered by Pierre and Marie Curie in 1898, was used for therapeutic applications until replaced by cobalt and cesium in the mid-1900s. Medical linear accelerators currently have mostly replaced source based teletherapy units due to dosimetric and safety advantages. Modern medical linear accelerators currently represent an integral part in managing oncological malignancies and other diseases.

1.2 Imaging as applied to radiotherapy

Precise anatomical localization is an important factor in accurately delivering dose to the target volume while sparing surrounding tissue in megavoltage (MV) radiation therapy. Currently, electronic portal imaging is the most common method of patient setup verification and localization, however, image quality is poor compared to kilovoltage images due primarily to the near absence of diagnostic energy photons. Current MV beams used for portal imaging purposes

are generated by full thickness, high atomic number (Z) targets. Due to the approximate Z^3 dependence of photoelectric interactions, a large fraction of the useful diagnostic quality photons in the energy range of 25 to 150 keV are absorbed within the target. Typically, these beams are then transmitted through a flattening filter which further hardens the beam. Orton and Robar¹ have shown that for a Varian accelerator operating in 6 MV mode, only 0.3% of all photons have energies between 25 and 150 keV, with the peak fluence occurring at approximately 500 keV. In the MV energy range, the dominant mode of photon interactions in tissue is Compton effect. Since Compton interactions are independent of Z, acquired MV images typically show poor contrast with little to no distinction between soft tissue types. Higher mean energies also lead to poor detection efficiency in the detector which results in poor contrast to noise ratios when compared to kilovoltage imaging for a given imaging dose.

1.3 Previous work on improving image guidance in radiotherapy

Various solutions to image guidance in radiotherapy have been adopted. Knight *et al*² have used an in-room CT on rails to verify patient position prior to treatment. Lagendijk *et al*³ have integrated an MRI with a medical accelerator for the same purpose. One rapidly growing method of image guidance is the use of orthogonally mounted kilovoltage (kV) systems. Jaffray *et al*⁴ reported on the suitability of these systems for use in kV cone-beam CT (CBCT) image guidance. They were able to demonstrate that a flat panel kV CBCT system adapted to a medical linear accelerator was able to produce images with excellent spatial resolution and contrast at acceptable doses. Various equipment manufacturers have since developed and implemented these designs. Sarfehnia *et al*⁵ have used orthogonal bremsstrahlung beams to produce x-ray spectrums of lower quality. These orthogonal beams were found to produce superior contrast when compared to the forward directed beams.

Other authors^{1, 6-9} have investigated using low-Z external targets in the absence of a flattening filter to produce beams with a high fraction of photons within the useful diagnostic energy range. When compared to dedicated kV systems, this option has the advantage of reduced mechanical complexity and cost as well as lower quality assurance requirements and the ability to capture beams-eye-view images. The primary focus of studies thus far has been on quantifying improvements in contrast and contrast to noise ratio due to the increased population of low energy photons in the spectra. The results have been promising with Orton and Robar¹ recently showing contrast improvement factors from 1.6 +/- 0.1 to 2.8 +/- 0.2 for 7 MeV electrons incident upon a 1 cm aluminum target, compared to the clinical 6 MV beam. All groups were able to acquire reasonably sharp images implying that spatial resolution was not significantly affected by their respective choices of targets. Flampouri *et al*⁹ were able to acquire sharp images despite the placement of the external target 15 cm beyond the nickel exit window. Roberts *et al*¹⁰ showed that for the target placement in Flampouri's experiment, the electron fluence distribution is 8 cm wide at the location of the target. It was also shown that for a 5 x 5 cm region located at isocenter, 71% of the photon energy fluence in Flampouri's results consisted of primary photons created within the nickel exit window of the primary collimator and only 28% came from the external carbon target.

Roberts *et al*¹⁰ characterized the spatial resolution of a full thickness 2 cm carbon target placed in a 4 MeV electron beam. Images of the line pair regions of the QC3 phantom (SeeDos Ltd. Bedfordshire, UK) were acquired using an XVI EPID (Elekta Ltd. Crawley, UK) for the custom target and compared to the clinical 6 MV mode with an iViewGT EPID (Elekta Ltd. Crawley, UK). An improvement in the MTF was observed for the custom target and XVI panel, however, as discussed by Roberts, the XVI panel does not contain a copper layer. This copper layer is used to increase the electron fluence in the scintillator, however, is

known to degrade spatial resolution due to lateral migration of electrons within the copper layer.

1.4 Research goals

The purpose of this work is to further explore the feasibility of imaging with low-Z targets by systematically investigating the spatial resolution dependence on various target parameters. In this work we vary three different design parameters of a low-Z target beam-line, including incident electron energy, target material and thickness to examine their effects on spatial resolution. This study compliments previously reported results on low-Z imaging with external targets to give a more complete view of the potential applications of such a system. We first investigate the MTF dependence upon the three target parameters using Monte Carlo simulation techniques. Experimental measurements are then carried out using an amorphous silicon based portal imager (aS1000/IAS3, Varian Medical, Inc.). The last phase of this research aims to investigate the potential advantages of using select low-Z targets in megavoltage cone-beam computed tomography (MV CBCT).

1.5 References

1. E. J. Orton and J. L. Robar, "Megavoltage image contrast with low-atomic number target materials and amorphous silicon electric portal imagers," *Phys. Med. Biol.* **54**, 1275-1289 (2009).
2. K. Knight, N. Touma, L. Zhu, G. Duchesne and J. Cox, "Implementation of daily image-guided radiation therapy using an in-room CT scanner for prostate cancer isocenter localization," *J Med Imaging Radiat Oncol* **53**, 132-138 (2009).
3. J. Lagendijk, B. Raatmakers, A. Raaijmakers, J. Overweg, K. Brown, E. Kerkhof, R. van der Put, B. Hardmark, M. van Vulpen and U. van der Heide, "MRI/linac integration," *Radiother Oncol* **86**, 25-29 (2008).
4. D. A. Jaffray, J. H. Siewerdsen, J. W. Wong and A. A. Martinez, "Flat-panel cone-beam computed tomography for image guided radiation therapy," *Int. J. Radiation Oncology Biol. Phys.* **53**, 1337-1349 (2002).
5. A. Sarfehnia, K. Jabbari, J. Seuntjens and E. B. Podgorsak, "Experimental verification of beam quality in high-contrast imaging with orthogonal bremsstrahlung photon beams," *Med. Phys.* **34**, 2896-2906 (2007).
6. D. M. Galbraith, "Low-energy imaging with high-energy bremsstrahlung beams," *Med. Phys.* **16**, 734-746 (1989).
7. A. Tsechanski, A. F. Bielajew, S. Faermann and Y. Krutmann, "A thin target approach for portal imaging in medical accelerators," *Phys. Med. Biol.* **43**, 2221-2236 (1998).
8. O. Z. Ostapiak, P. F. O'Brien and B. A. Faddegon, "Megavoltage imaging with low Z targets: implementation and characterization of an investigational system," *Med. Phys.* **25**, 1910-1918 (1998).
9. S. Flampouri, P. M. Evans, F. Verhaegen, A. E. Nahum, E. Spezi and M. Partridge, "Optimization of accelerator target and detector for portal imaging using Monte Carlo simulation and experiment," *Phys. Med. Biol.* **47**, 3331-3349 (2002).
10. D. A. Roberts, V. N. Hansen, A. C. Niven, M. G. Thompson, J. Seco and P. M. Evans, "A low Z linac and flat panel imager: comparison with the conventional imaging approach," *Phys. Med. Biol.* **53**, 6305-6319 (2008).

Chapter 2

BEAM PRODUCTION AND PARTICLE INTERACTIONS

2.1 INTRODUCTION.....	6
2.2 INTERACTIONS OF CHARGED PARTICLES WITH MATTER	6
2.2.1 <i>General aspects of Coulomb interactions</i>	6
2.2.2 <i>Stopping power</i>	8
2.2.3 <i>Range of charged particles</i>	11
2.2.4 <i>Production of x-rays</i>	12
2.3 PHOTON INTERACTIONS WITH MATTER.....	15
2.3.1 <i>Compton scattering</i>	15
2.3.2 <i>Photoelectric effect</i>	18
2.3.3 <i>Pair production</i>	20
2.4 BEAM PRODUCTION IN MODERN MEDICAL LINEAR ACCELERATORS.....	22
2.5 REFERENCES	26

2.1 Introduction

In this chapter we introduce the various interactions between the particles of interest in megavoltage radiotherapy and imaging. Charged particle interactions are first discussed, followed by photon interactions.

2.2 Interactions of charged particles with matter

2.2.1 General aspects of Coulomb interactions

As charged particles travel through a medium they experience Coulomb interactions with orbital electrons and the nucleus of the absorber material. The Coulomb force (F_{Coul}) is given by

$$F_{Coul} = \frac{q_1 q_2}{4\pi\epsilon_0 r^2} \quad (2.1.)$$

where

q_1 is the charge of interacting particle

q_2 is the charge of the interaction partner

ϵ_0 is the permittivity of vacuum in free space (8.854×10^{-12} C/Vm)

r is the distance between the two particles

These particles will typically undergo a number of elastic and inelastic interactions before coming to rest. The nature of the interactions can be broken down into three main types based upon the size of the classical impact parameter b compared to the atomic radius a . These parameters for the three different collision types are illustrated in Fig. Figure 2.1 and are described below.

- 1. Soft collisions.** Interactions of a charged particle with an orbital electron. In this case the impact parameter is much larger than the atomic radius ($b \gg a$).
- 2. Hard collisions.** Interactions of a charged particle with the orbital electron. In this case, the impact parameter is similar in magnitude to the atomic radius ($b \approx a$). A much greater fraction of the charged particles energy is transferred to the orbital electrons than in soft collisions. The orbital electrons may gain sufficient kinetic energy to leave the region of interest and in this case are termed delta rays.

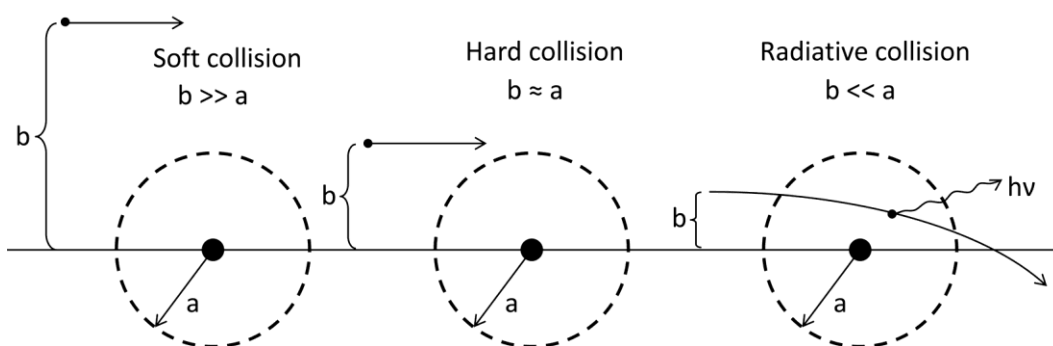


Figure 2.1: The three different types of charged particle interactions with an atom. Hard, soft and radiative collisions are defined by the size of the impact parameter (b) relative to the atomic radius.

3. Radiative collisions. For these interactions, the charged particle interacts directly with the external nuclear field of the nuclei ($b \ll a$). In this instance, the Coulomb force causes an acceleration that causes the charged particle to release some of its energy in the form of a bremsstrahlung photon.

2.2.2 Stopping power

The linear stopping power (dE/dx) describes a charged particle's rate of energy loss (dE) as a function of path length (dx) in the medium and has units of MeV/cm. The charged particle's energy loss is a result of the hard, soft and radiative interactions discussed above. These energy losses are typically divided into two main types: i) collisional stopping power (S_{col}) and ii) radiative stopping power. The total linear stopping power (dE/dx) is then the sum of the two types. To remove dependencies on absorber density (ρ), the total linear stopping power can be divided by the density of the absorber. This normalized total stopping power is termed the mass stopping power (S_{tot}) and is written as

$$\frac{dE}{\rho dx} = S_{tot} = S_{col} + S_{rad} \quad (2.2.)$$

The mass collisional stopping power (S_{col}) represents the energy losses by charged particles through ionization and excitation of the absorber atom. This energy loss is the result of hard and soft interactions and represents an elastic collision that results in dose deposition relatively close to the track of the charged particle. The mass collisional stopping power as given by the ICRU Report 37¹, is

$$S_{col} = 2\pi r_e^2 \frac{Z}{A} N_A \frac{m_e c^2}{\beta^2} \left[\ln \left(\frac{E_k}{I} \right)^2 + \ln(1 + \tau/2) + F^\pm(\tau) - \delta \right], \quad (2.3.)$$

where

r_e is the classical electron radius,

Z is the atomic number of the atom,

A is the number of nucleons,

- N_A is the Avogadro's number
 m_e is the mass of the electron,
 β is the speed of the charged particle divided by the speed of light in vacuum (v/c),
 E_k is the kinetic energy of the light charged particle,
 I is the mean excitation potential,
 τ is the electron or positron kinetic energy normalized to $m_e c^2$,
 δ is the polarization correction.

The function $F^\pm(\tau)$ differs depending upon the charge of the particle. For electrons it is defined as

$$F^-(\tau) = (1 - \beta^2)[1 + \tau^2/8 - (2\tau + 1) \ln 2], \quad (2.4.)$$

and for positrons is

$$F^+(\tau) = 2 \ln 2 - (\beta^2/12) \left[23 + \frac{14}{\tau + 2} + \frac{10}{(\tau + 2)^2} + \frac{4}{(\tau + 2)^3} \right]. \quad (2.5.)$$

The minimum energy transferred per interaction is limited by the binding energy of an electron or the excitation potential required to excite that electron into a higher shell. The maximum energy transferred per interaction is limited by the classical maximum energy transfer in a head on collision of two particles of equal mass and is equal to the kinetic energy of the incident particle or half the kinetic energy of the incident particle depending upon whether the two particles are distinguishable or indistinguishable respectively.

The mass radiative stopping power (S_{rad}) describes the rate of bremsstrahlung production of light charged particles. This process does not apply to heavy charged particles due to the fact that their relatively heavy mass prohibits the accelerations required to satisfy radiation emission governed by the Larmor relationship. S_{rad} is defined as²

$$S_{rad} = N_a \sigma_{rad} E_i \quad (2.6.)$$

where

N_a is the number of atoms per unit mass ($N_a = N/m = N_A/A$)

σ_{rad} is the total cross section for bremsstrahlung production

E_i is the initial total energy of the light charged particle.

The total cross section σ_{rad} differs depending upon whether the velocity of the charged particle is relativistic or not. For relativistic particles ($E_k \ll m_e c^2$), σ_{rad} is defined as $(16/3)\alpha r_e^2 Z^2$. Substitution into equation 2.6. yields

$$S_{rad} = \alpha r_e^2 Z^2 \frac{N_A}{A} B_{rad} E_i \quad (2.7.)$$

where

B_{rad} is defined as $\sigma_{rad}/\alpha r_e^2 Z^2$ and has a value of 16/3 for light charged particles in the non-relativistic energy range. The value of B_{rad} is approximately 6 at $E_k = 1 \text{ MeV}$, 12 at $E_k = 10 \text{ MeV}$ and 15 at $E_k = 100 \text{ MeV}$.²

As Z/A is relatively constant at 0.5, S_{rad} is proportional to Z as well as the initial total energy of the light charged particle. Figure 2.2 shows the plot of mass collision and mass radiative stopping powers for water, aluminum and lead.

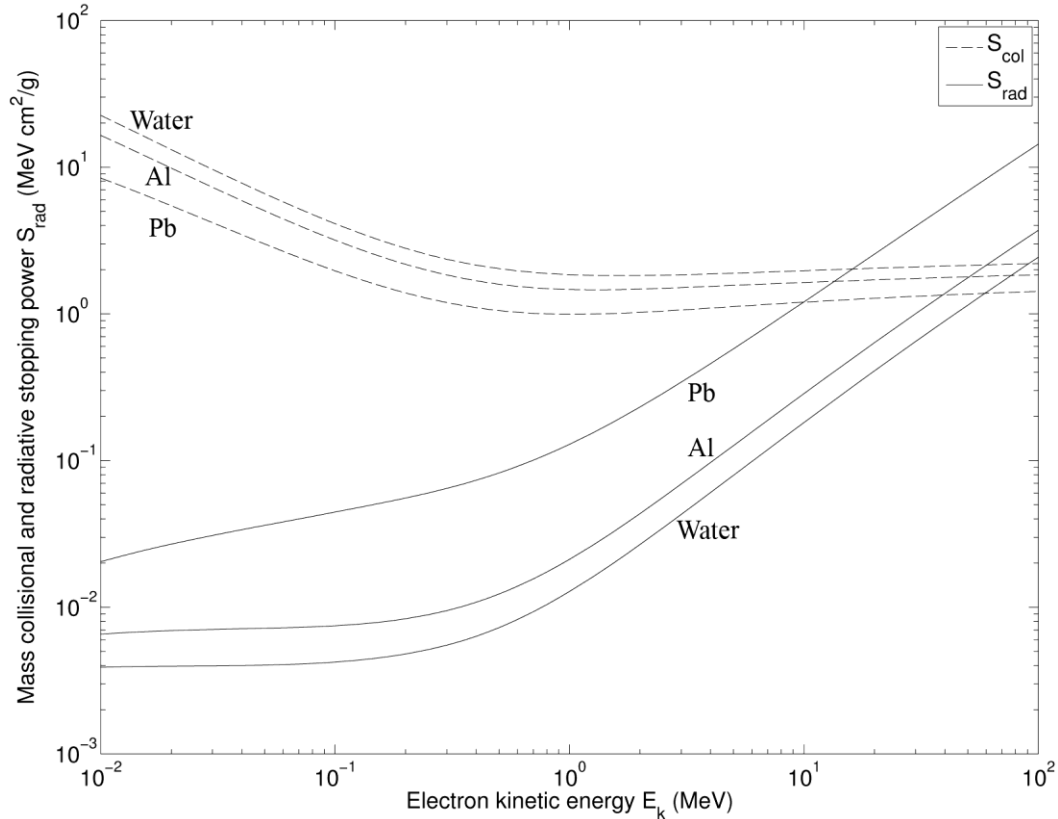


Figure 2.2: The mass collision (dashed lines) and mass radiative (solid lines) stopping power for electrons and positrons in three different materials.

2.2.3 Range of charged particles

As discussed, particles traversing a medium lose their kinetic energy through absorption, ionization and radiative losses. This results in a finite range for charged particles in a particular medium. For individual interactions of heavy charged particles, their relatively high mass prohibits large angular deflections and their trajectory is relatively straight. However, light charged particles have trajectories through media that can be quite torturous. Since these light charged particles tend to undergo large angular deviations in their track, their actual depth of penetration (range) is typically less than the integrated path length along its track. The mean path length can be approximated using the continuous slowing down approximation (CSDA) described as

$$R_{CSDA} = \int_0^{E_{K_i}} \frac{dE}{S_{tot}(E)}, \quad (2.8.)$$

where

R_{CSDA} is the CSDA range (mean path length) of the of the charged particle,

E_{K_i} is the initial kinetic energy of the particle,

$S_{tot}(E)$ is the total mass stopping power as a function of the kinetic energy.

2.2.4 Production of x-rays

The main method of x-ray production in medical linear accelerators is through the acceleration of charged particles (bremsstrahlung production). To describe the intensity of radiation emitted from a charged particle (energy flux), the Poynting vector can be used. It is defined as

$$\vec{S} = \vec{E} \times \vec{B} / \mu_0, \quad (2.9.)$$

where

\vec{E} is the electric field,

\vec{B} is the magnetic field

μ_0 is the magnetic permittivity of vacuum

Recognizing that the electric and magnetic field are perpendicular and substituting them into equation 2.1. yields

$$|\vec{S}| = \frac{EB}{\mu_0} = \frac{1}{16\pi^2\epsilon_0} \frac{q^2 a^2 \sin^2 \theta}{c^3 r^2}, \quad (2.10.)$$

where

ϵ_0 is the permittivity of vacuum,

q is the charge of the accelerated particle,

a is the acceleration of the particle,

c is the speed of light in vacuum,

θ is the angle between the particles velocity vector and the radius vector connecting the charged, particle with the point of observation,

r is the distance between the particle and the point of observation.

This result indicates that the intensity of emitted radiation will be proportional to the square of the particle's charge and the square of the particle's acceleration. It also shows that the intensity of emitted radiation will exhibit a maximum at right angles and zero in the forward and backward direction. However, for relativistic particles, the electric field is distorted and as a result, the emitted radiation intensity also becomes distorted. For relativistic particles the Poynting vector becomes

$$|\vec{S}| = \frac{1}{16\pi^2\epsilon_0} \frac{q^2 a^2}{c^3 r^2} \frac{\sin^2 \theta}{(1 - \beta \cos \theta)^5}, \quad (2.11.)$$

where β represents the particle's velocity normalized to the speed of light in vacuum (c).

As the particle reaches relativistic speeds, the angle of maximum intensity tips forward. This angle of maximum intensity is called the characteristic angle (θ_{max}). By differentiating the Poynting vector with respect to θ and setting the equation to zero, it is possible to determine the characteristic angle,

$$\theta_{max} = \cos^{-1} \left[\frac{1}{3\beta} \left(\sqrt{1 + 15\beta^2} - 1 \right) \right]. \quad (2.12.)$$

Electron vacancies can be created within the atom through various means including: i) Photoelectric effect, ii) Compton scattering, iii) Triplet Production, iv) Charged particle interactions, v) Internal conversion, vi) Electron capture, vii) Positron annihilation and viii) Auger effect. When found in inner shells, these vacancies represent an excited state for the atom which will cause orbital electrons to undergo a series of transitions to return to the ground state. As the atom undergoes relaxation, the difference in energy between the excited state and ground state is emitted in one of the following ways: i) radiatively as characteristic x-rays or, ii) non-radiatively as Auger electrons.

The Auger effect results when the transition energy is transferred to another electron which is subsequently ejected from the atom. The energy of this electron will be the transition energy minus the binding energy of the Auger electron.

Radiative losses from electron transitions into lower energy states are also possible. These radiated photons (termed characteristic x-rays) will have an energy that is equal to the binding energy of the electron in its initial state minus the binding energy of the electron in its final state. However, unlike Auger effect, only certain allowed transitions will produce a characteristic x-ray.

The fluorescent yield ω represents the number of characteristic photons that will be emitted per vacancy. Figure 2.3² shows the fluorescent yield for k shell (ω_K) and l shell (ω_L) vacancies plotted as a function of atomic number Z. Also included in this graph is the fraction of all photoelectric interactions (P_K) that occur in the K shell for $h\nu > (E_B)_K$ and L shell (P_L) for $h\nu > (E_B)_L$.

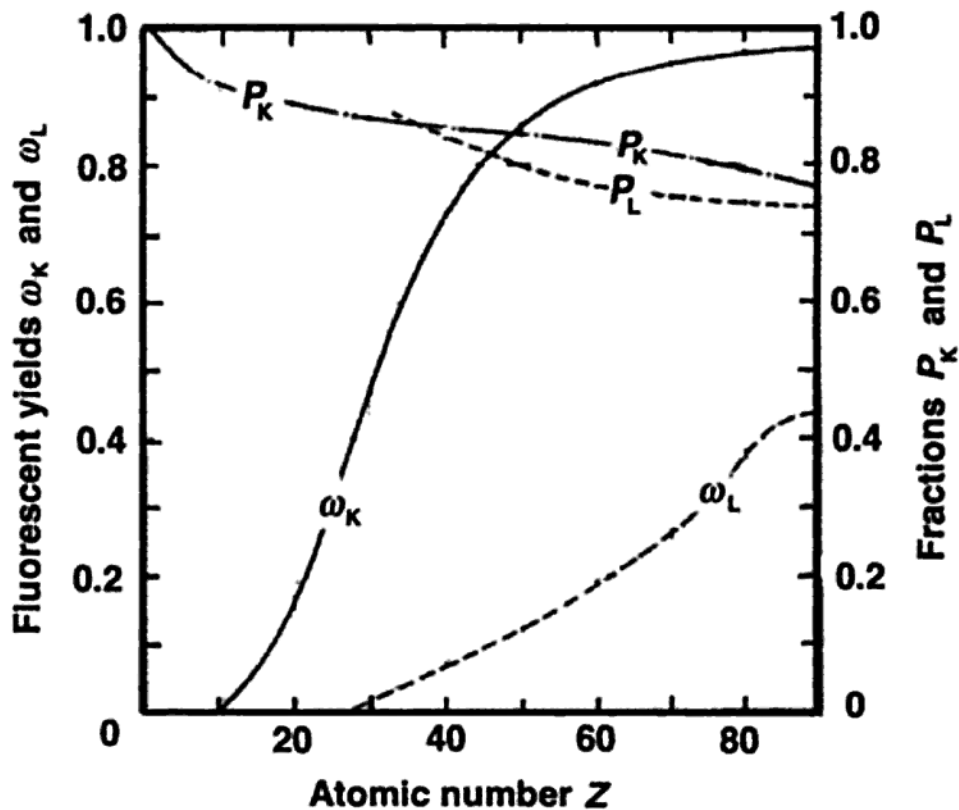


Figure 2.3: The fluorescent yield for the k (ω_k) and l (ω_l) shells plotted against atomic number Z. The fraction of all photoelectric interactions that occur in the K shell (P_K) for $h\nu > (E_B)_K$ and in the L shell (P_L) for $h\nu > (E_B)_K$.

2.3 Photon interactions with matter

As photons traverse any medium they have a certain probability of interacting with the atoms in that medium. The most prominent interaction types in megavoltage radiation therapy are photoelectric effect, Compton scattering, and pair production. Thompson scattering, Rayleigh scattering and photonuclear reactions also occur at these energies, however, play a comparatively minor role in dose deposition and megavoltage imaging and will not be discussed here.

2.3.1 Compton scattering

Compton scattering is the incoherent scattering of an incident photon with a loosely bound orbital electron. For sufficiently large incident photon energies the

electron is assumed to be free and stationary; however, as the incident photon energy approaches the binding energy of the electron, the approximation breaks down. Figure 2.4 shows a typical Compton interaction where an incident photon ($h\nu$) interacts with a free and stationary electron.

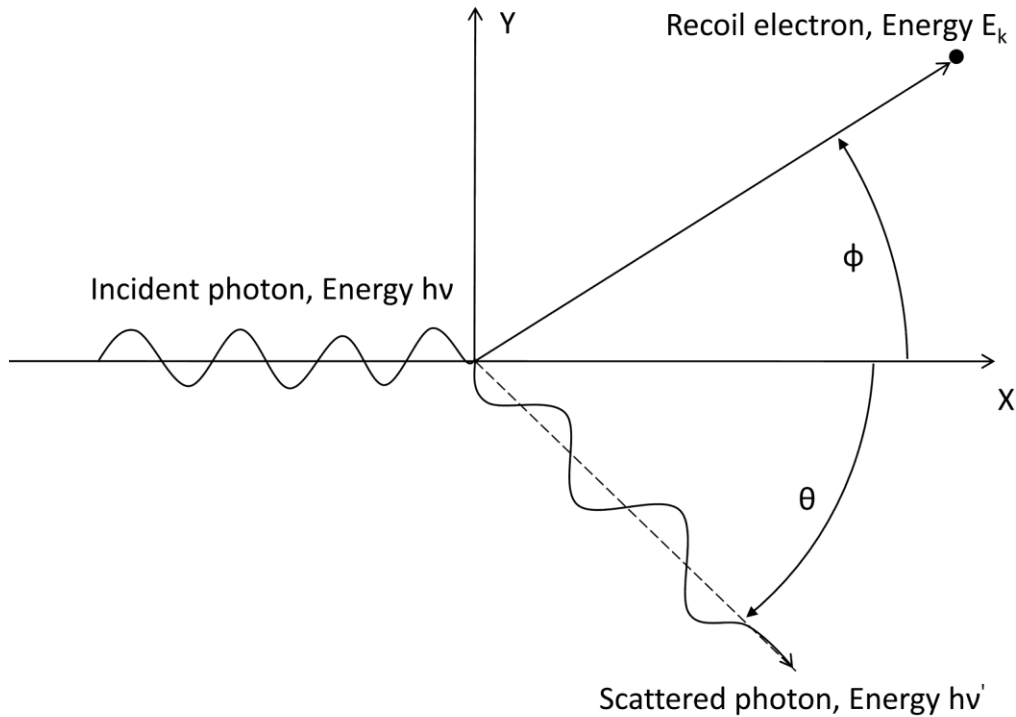


Figure 2.4: A schematic representation of a Compton interaction in which an incident photon scatters off of an orbital electron.

The photon is scattered at an angle θ and emerges with a reduced energy $h\nu'$. The recoil (Compton) electron is scattered at an angle ϕ and has a kinetic energy E_k . The energy of the scattered photon ($h\nu'$) and electron (E_k) are given by,

$$h\nu' = h\nu \frac{1}{1 + \varepsilon(1 - \cos\theta)}, \quad (2.13.)$$

and

$$E_k = h\nu \frac{\varepsilon(1 - \cos\theta)}{1 + \varepsilon(1 - \cos\theta)}, \quad (2.14.)$$

where $\varepsilon = h\nu/m_e c^2$. Equation 2.13 highlights a few important aspects of this interaction type. For very small scattering angles ($\theta \approx 0$), the energy of the scattered photon is similar to the energy of the incident photon. For increasing scattering angles, the energy of the scattered photon will decrease relative to the incident photon energy. For photon scattering angles of π and $\pi/2$, the maximum scattered photon energy is 0.256 and 0.511 MeV respectively, regardless of the incident photon energy. From equation 2.14 the average fraction of energy transferred to the recoil electron increases for increasing incident photon energy.

The relationship between θ and ϕ can be represented as

$$\cot \phi = (1 + \varepsilon) \tan \theta / 2 . \quad (2.15.)$$

The probability (cross section) for a Compton interaction occurring is represented as the total electronic Klein-Nashina cross section (${}_e\sigma_c^{KN}$). This is defined as²

$${}_e\sigma_c^{KN} = 2\pi r_e^2 \left\{ \frac{1 + \varepsilon}{\varepsilon^2} \left[\frac{2(1 + \varepsilon)}{1 + 2\varepsilon} - \frac{\ln(1 + 2\varepsilon)}{\varepsilon} \right] + \frac{\ln(1 + 2\varepsilon)}{2\varepsilon} - \frac{1 + 3\varepsilon}{(1 + 2\varepsilon)^2} \right\}, \quad (2.16.)$$

where

r_e is the classical electron radius,

ε is $h\nu/m_e c^2$.

Since Compton interactions are assumed to take place with free and stationary electrons (they are not bound to the nucleus), the total electronic cross section is independent of the atomic number Z. The atomic cross section (${}_a\sigma_c^{KN}$) is then defined as the electronic cross section multiplied by Z (${}_a\sigma_c^{KN} = Z {}_e\sigma_c^{KN}$) and the Compton mass attenuation coefficient is then defined as

$$\frac{\sigma_c^{KN}}{\rho} = \frac{N_A}{A} {}_a\sigma_c^{KN} = \frac{ZN_A}{A} {}_e\sigma_c^{KN} \approx 0.5N_A {}_e\sigma_c^{KN}, \quad (2.17.)$$

where

ρ is the density of the medium

N_A is Avogadro's number

A is the number of nucleons

Z is the atomic number

It follows from equation 2.17 that the atomic cross section is linearly proportional to Z and the Compton mass attenuation coefficient is essentially independent of Z .

2.3.2 Photoelectric effect

Photoelectric effect represents a photon interaction with a tightly bound electron. Interactions are more likely in the inner shells as the atom as a whole must take up the difference in momentum between the incident photon and the ejected electron (photoelectron). Unlike Compton interactions, the photon is absorbed completely and its energy is transferred to the electron minus the electron binding energy. The kinetic energy of the photoelectron E_k is then written as

$$E_k = h\nu - E_B \quad (2.18.)$$

where

$h\nu$ is the energy of the incident photon,

E_B is the binding energy of the tightly bound electron.

The atomic cross section for photoelectric effect varies depending upon the energy of the incident photon. For regions close to the absorption edges, the atomic cross section for K-shell photons is given as

$${}_a\tau_K = \alpha^4 e\sigma_{Th}Z^n \sqrt{\frac{32}{\epsilon^7}}, \quad (2.19.)$$

where

α is the fine structure constant,

${}_e\sigma_{Th}$ is the total Thomson electric cross section,
 n is the power of the Z dependence (n=4 for relatively low photon energies to n=4.6 for higher photon energies).

In the relativistic region, the atomic cross section for K-shell electrons is defined as

$${}_a\tau_K = \frac{1.5}{\varepsilon} \alpha^4 Z^5 {}_e\sigma_{Th}. \quad (2.20.)$$

It is important to note the high Z dependence of the atomic cross section which varies between 4 (for relatively low energy photons) and 5 (for relatively high energy photons).

The average energy transferred to electrons is given by

$$\overline{E}_{tr}^\tau = h\nu - P_K \omega_K \overline{h\nu}_K \quad (2.21.)$$

where

P_K is the fraction of all photoelectric interaction that occur in the K shell. P_K is plotted in Figure 2.3 and slowly varies as a function of Z at a value of around 0.85.

ω_K is the fluorescent yield for the K-shell

$\overline{h\nu}_K$ is the weighted mean energy radiated following electron transitions to the K-shell.

The $P_K \omega_K \overline{h\nu}_K$ term in equation 2.21 corrects for additional energy imparted to electrons through the Auger process as atomic relaxations begin to fill the vacancy created in the initial interaction. In general, the kinetic energy transferred to electrons is between $h\nu - E_B$ (no Auger electrons are emitted) and $h\nu$ (no characteristic x-rays are emitted).

The mass attenuation coefficient for photoelectric effect is then related to the atomic cross section by

$$\frac{\tau}{\rho} = \frac{N_A}{A} {}_a\tau, \quad (2.22.)$$

The mass photoelectric coefficient varies between Z^4 for low Z absorbers and Z^3 for high Z absorbers.

2.3.3 Pair production

Pair production is a type of photon interaction that can occur in the Coulomb field of an atomic nucleus or an orbital electron. For these events the photon is absorbed and its energy is transferred into an electron-positron pair as illustrated schematically in Figure 2.1.

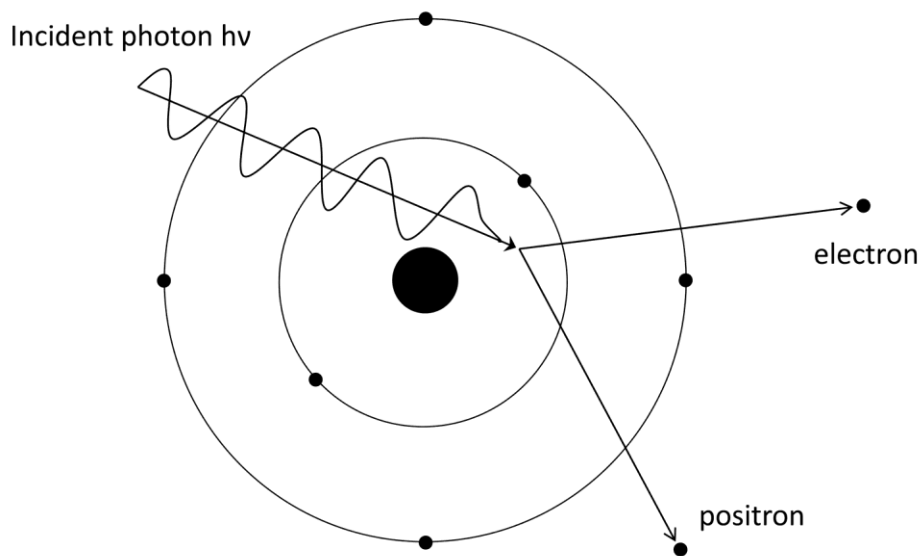


Figure 2.5: A representation of a pair production interaction in which an incident photon interacts with the Coulomb field of an atomic nucleus. Its energy is transferred into the creation of an electron-positron pair.

For these interactions, conservation of charge, energy and momentum must occur. Charge is conserved due to the equal and opposite charge of the electron-positron pair. Energy is conserved through the complete transfer of the incident photon's energy into the total energy of the positron plus electron. The requirement for momentum conservation dictates that the event must happen within the Coulomb field of an atomic nucleus or electron such that the nucleus or electron may take up the momentum of the incident photon. In the event that the interaction occurs with an orbital electron as opposed to the nucleus, the

transferred momentum may be sufficient to eject the electron from the atom. In this case, the particles present after the interaction will include the electron-positron pair and the ejected orbital electron. This is referred to as triplet production and is a special case of pair production.

As the electron and positron both have a rest mass of 0.511 MeV. The energy required to create these particles must come from the incident photon. This implies that there is a threshold energy for pair production events and that it should be roughly twice the rest energy of the electron. The threshold energy is calculated as

$$E_{\gamma thr}^{pp} = 2m_e c^2 \left(1 + \frac{m_e c^2}{m_A c^2} \right), \quad (2.23.)$$

where

$m_e c^2$ is the rest mass of the electron,

$m_A c^2$ is the rest mass of the atom.

Since the electron rest mass is much smaller than the rest mass of the atom, the threshold energy is approximately $2m_e c^2$.

The threshold energy for triplet production is defined as

$$E_{\gamma thr}^{pp} = 4m_e c^2. \quad (2.24.)$$

The atomic cross section for pair production is given as

$${}_a\kappa = \alpha r_e^2 Z^2 P(\varepsilon, Z), \quad (2.25.)$$

where

α is the fine structure constant,

r_e is the classical electron radius,

Z is the atomic number,

$P(\varepsilon, Z)$ is a function of photon energy $h\nu$ and atomic number Z ,

and the mass attenuation coefficient is then written as follows

$$\frac{\kappa}{\rho} = \frac{N_A}{A} a\kappa. \quad (2.26.)$$

It can be seen from equations 2.25 and 2.26 that the atomic cross section varies approximately as a function of Z^2 and the mass attenuation coefficient varies approximately linearly as a function of the atomic number of the absorber.

The total kinetic energy transferred to charged particles in a single pair production interaction is simply the incident photon energy minus the rest mass of the two charged particles,

$$(E_K^k)_{tr} = h\nu - 2m_e c^2. \quad (2.27.)$$

The created positron is identical to the electron except that it has equal but opposite charge. The positron will travel through the medium depositing its kinetic energy through ionization and excitation interactions until it comes to rest. Once at rest, it will combine temporarily with an electron to form a metastable structure called positronium. The electron-positron pair will then annihilate creating two annihilation photons of 0.511 MeV that move off in opposite directions. A special case of positron annihilations exists where a positron of non-zero kinetic energy annihilates with an electron. This is termed annihilation in flight and represents only about 2% of all annihilation interactions.

2.4 Beam production in modern medical linear accelerators

External beam radiotherapy is routinely delivered using medical linear accelerators. Modern accelerators are capable of producing photon beams between 4 MV and 25 MV. Figure 2.6 shows a block diagram of a modern medical linear accelerator³.

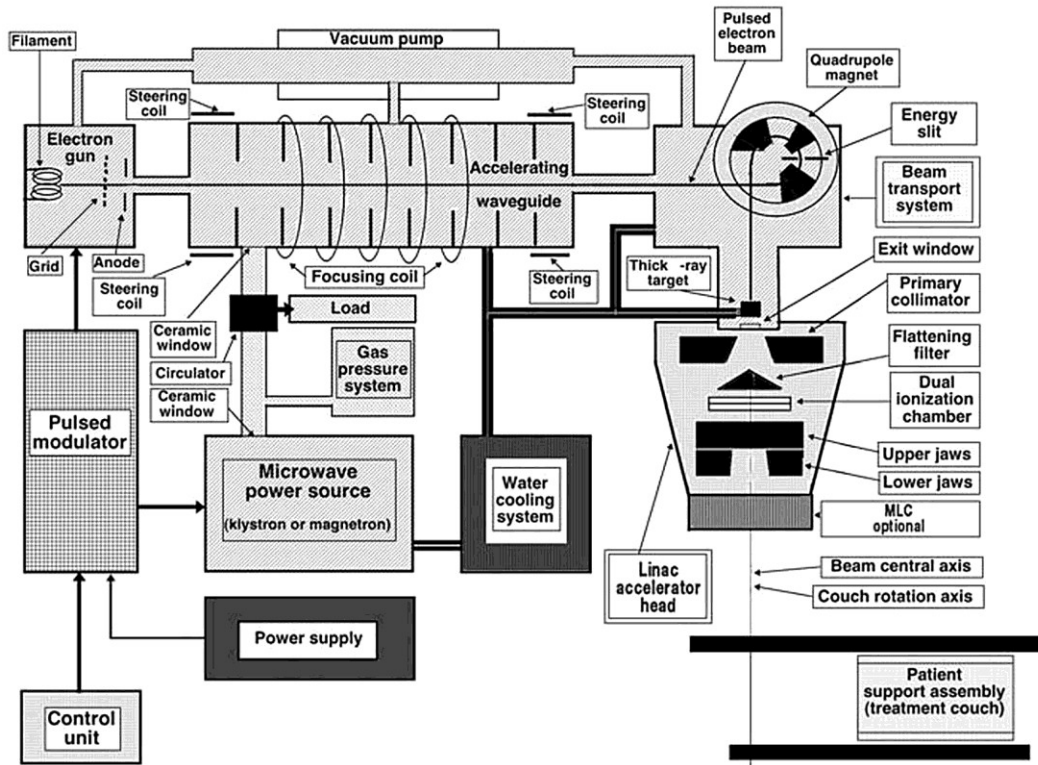


Figure 2.6: A block diagram of a modern medical linear accelerator ³.

The production of megavoltage photon beams first starts with the acceleration of electrons. Electrons are emitted into vacuum through thermionic emission from an electron gun and accelerated in bunches through a static potential (typically 20 kV) into the main accelerating wave guide. High power RF is fed into the evacuated waveguide by a magnetron or klystron most commonly at a frequency of 2856 MHz. The electrons are then accelerated along the length of the waveguide such that they are repeatedly exposed to an electrical potential that further accelerates them in the direction of motion. In higher energy accelerators, the particles typically then move into a beam transport system where they are magnetically steered such that they will impact the target in the desired orientation. The electron beam then enters the accelerator head which is diagrammed schematically in Figure 2.6 and for the production of photon beams, strikes a high atomic number transmission target. This process produces a photon shower through bremsstrahlung production and characteristic x-rays

which results in a polyenergetic beam with photon energies as high as the nominal energy of the incident electron beam. All electrons are typically stopped within the thick target and the photons continue down through a primary collimation device. They then make the transition from vacuum to air by passing through an x-ray exit window which varies in thickness and material depending upon the manufacturer. The beam then passes through a flattening filter to account for its forward peaked nature and higher mean energy along central axis in order to produce a homogeneous dose distribution within the inner 80% of the largest field size available (typically $40 \times 40 \text{ cm}^2$) at a depth of 10 cm in water and a source to surface distance of 100 cm. In order to quantify the dose delivered to the patient, the beam then passes through a dual ionization chamber. This component measures the output of the unit as well as determining the flatness and symmetry of the beam. The delivered dose rate of the accelerator is controlled by a feedback loop between the measured current from the ion chamber and the electron gun current. Output is determined by integrating this current over time such that a certain integrated signal (monitor unit or MU) is related to the dose delivered to a water phantom. The output is adjusted under reference conditions (commonly a $10 \times 10 \text{ cm}^2$ field at 100 cm source to surface distance and at the depth of maximum dose for that particular beam) such that $1 \text{ cGy} = 1 \text{ MU}$. The beam then passes through a mirror used to project a light field used to help visually position objects with respect to the isocenter and to help identify the field edge. The beam is then collimated further by secondary collimation that consists of two orthogonal sets of independent jaws. The faces of the jaws move along an arc such that their edge is parallel to the divergent photon beam at all field sizes. This helps to maintain a sharp transition between the inside and outside of the treatment field. Primary transmission through the jaws should not exceed 2% of the open field value as defined by the International Electrotechnical Commission. Modern accelerators are also equipped with tertiary photon collimation in the form of a multileaf

collimator (MLC). This device allows for the definition of irregularly shaped fields. The photon beam then passes through a Mylar window which is used to keep foreign matter outside the treatment head as well as to project a crosshair shadow which helps in identifying the isocenter as well as the rotation of the rectangular field. Most high energy accelerators are also capable of delivering electron treatments with nominal energies as low as 4 MeV and as high as 22 MeV. These beams are produced in a similar manner as the photon beams, however with a few key differences. In electron mode, the therapy bremsstrahlung target is retraced and the electron pencil beam travels through the primary collimator and down to the carousel which normally holds the flattening filter. In these modes the flattening filter is removed from the beam and is replaced by a high atomic number thin foil used to scatter the electrons in order to create a roughly divergent beam. Secondary collimation is again provided by the jaws, however, the MLC is not used for electron collimation and is replaced by an electron applicator that provides electron collimation to within a few cm (typically 5 to 20 cm) of the patient surface.

2.5 References

1. ICRU, "Stopping powers for electrons and positrons," ICRU Report 37 (1984).
2. E. B. Podgorsak, *Radiation Physics for Medical Physicists*. (Springer, 2006).
3. E. B. Podgorsak, *Radiation Oncology Physics: A Handbook for Teachers and Students*. (IAEA, 2005).

Chapter 3

RADIATION DOSIMETERS AND DETECTION DEVICES

3.1 INTRODUCTION.....	27
3.2 FILM MEASUREMENTS	27
3.3 ELECTRONIC PORTAL IMAGING DEVICES	29

3.1 Introduction

Radiation dosimeters are devices that are capable of measuring the various dosimetric quantities including exposure, kerma and absorbed dose. Certain types of dosimetry systems including calorimetry, Fricke dosimeters and ionization chambers, directly measure the absorbed dose to water and are referred to as absolute dosimeters. Other dosimetry systems are capable of relative dosimetric measurements and include radiographic film, thermoluminescent dosimeters and diodes.

Film and diode arrays are special cases in that they are capable of measuring the absorbed dose at multiple points within a two dimensional plane to form images. Film has been used since the advent of radiography to record projections of patient anatomy, but is currently being phased out in favour of digital detection systems. In this chapter we introduce these basic imaging systems.

3.2 Film measurements

Since the advent of radiography which started with Roentgen's discovery of x-rays in 1895, film detection systems have long been the standard in anatomical imaging. For megavoltage imaging applications, x ray film typically consists of a plastic base layer that is coated on both sides by a radio-sensitive emulsion layer. A schematic representation of the film layers can be seen in Figure 3.1.

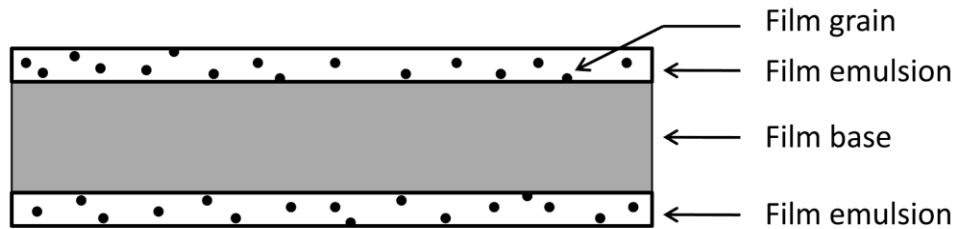


Figure 3.1: A schematic representation of film layers.

The emulsion typically consists of silver bromide (AgBr) grains that are suspended in a supporting material. Upon exposure to radiation, ionization of the film grains produces a latent image that must be chemically processed in order to render the image visible. Light transmission through the film is then used as a measure of film exposure as regions of higher exposure will typically have higher optical density after processing. The optical density is defined as

$$OD = \log_{10} \frac{I_o}{I}, \quad (3.1.)$$

where

I_o is the initial light intensity,

I is the light intensity transmitted through the film.

The relation between exposure and optical density is represented by the characteristic curve as seen in Figure 3.2.

The base plus fog portion of the characteristic curve represents the film opacity due to the film base and emulsion layers plus any darkening to the emulsion layer due to exposure from natural background radiation. This region, along with the region above the shoulder, has a relatively shallow slope and falls outside the useful range of exposures. The width of the linear region represents the useful range of film exposures and is referred to as the latitude or the dynamic range. The slope of this linear region is termed the film speed or gamma.

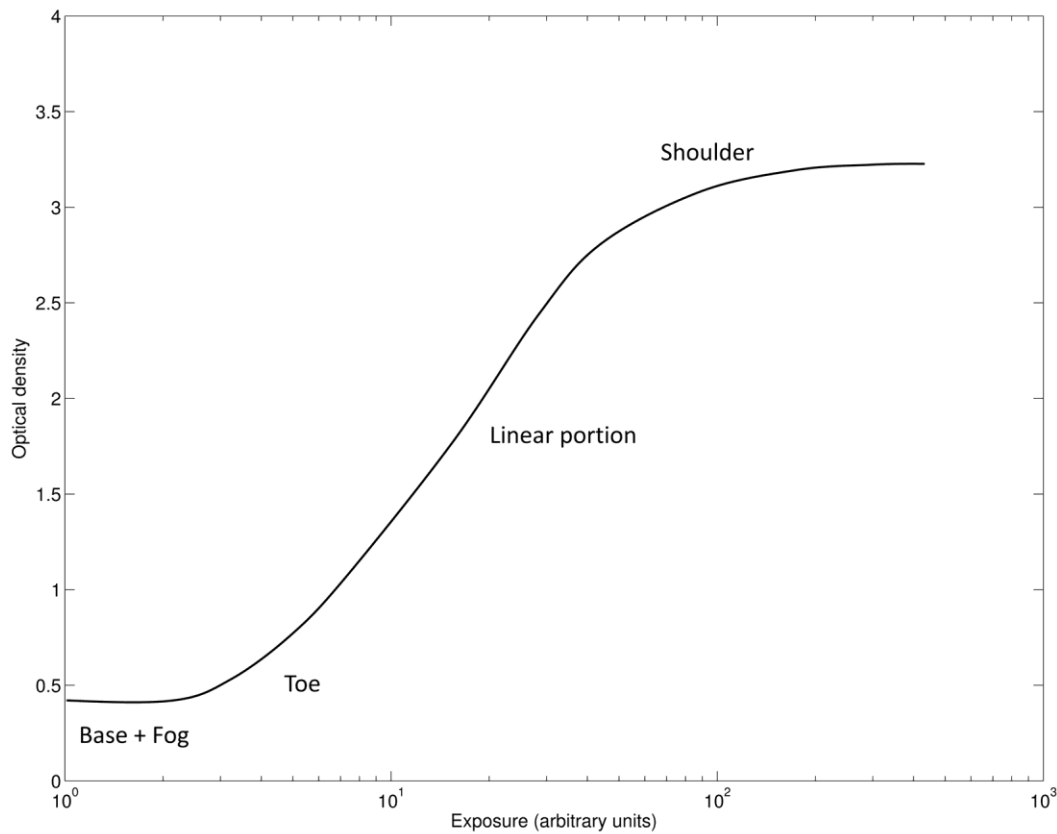


Figure 3.2: A typical optical density curve as a function of exposure.

Radiochromic film represents a special type of film that does not need special processing to reveal the latent image. These films contain a monomer that polymerizes upon exposure to ionizing radiation which causes the optical density to increase. Light transmission can then be related to dose through a dosimetric curve as in the case of radiographic film.

3.3 Electronic portal imaging devices

Digital x-ray detection has largely replaced film as the primary image verification method in MV portal imaging. These digital detectors are referred to as electronic portal imaging devices (EPID). Current generations of EPID panels employ active matrix, indirect detection. A schematic diagram of the detection process is outlined in Figure 3.3.

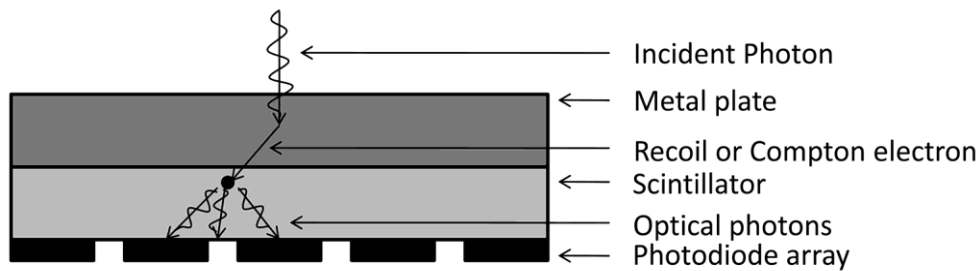


Figure 3.3: A schematic representation of the most common photon detection process in a modern electronic portal imaging device (EPID). The photon first passes into a metal plate and sets into motion an electron that interacts with a scintillator. Optical photons are emitted from the scintillator and are detected by a photodiode array.

Modern EPIDs consist of three main functional layers. (1) A metal buildup plate (typically copper) that is designed to induce Compton or photoelectric interactions from the incident MV photon beam. The thickness of the plate is optimized to be great enough to have a high probability of photon interaction yet thin enough to allow the secondary particles to have sufficient kinetic energy to reach the scintillator. (2) The secondary particles then interact with a scintillation material whose orbital electrons are excited through collision interactions with the incident electron. The subsequent de-excitation then emits photons in the visible spectrum. (3) These photon emissions are detected by photodiodes deposited on a glass substrate. A thin film transistor is coupled to the diode and acts as a switch to for reading the integrated signal.

For the purposes of this research, a Varian aS1000 (Varian Medical, Inc.) imager was used. It consists of a 1024 x 768 amorphous silicon (aSi) photodiode array with individual pixel dimensions of 0.39 x 0.39 mm². The total imaging area was 30 x 40 cm. The buildup layer consisted of 1 mm of copper and the scintillator was a Gd₂O₂S:Tb phosphor layer.

Chapter 4

MONTE CARLO SIMULATION OF PARTICLE INTERACTIONS

2.1	Introduction	31
2.2	EGSnrc and the BEAM code system.....	32
2.3	Improving efficiency in Monte Carlo simulations.....	34
2.4	References	36

4.1 Introduction

The Monte Carlo method is a very powerful and useful tool for medical physicists. It is the de facto standard in dose calculations of photon and electron beams; however, its adoption into routine clinical practice has been slow due to the long computational times involved. Recent advances in computational power per unit cost have facilitated practical incorporation into commercial treatment planning systems^{1,2}.

Monte Carlo methods rely on repeatedly using pseudo randomly generated numbers to determine the result of stochastic events. The Monte Carlo method of particle transport is a conceptually simple process. Source particle parameters are specified in the input file and are then tracked through the simulation geometry that is specified by the user. As particles traverse a medium, their range, specific interaction types, scattering angle and energy loss are not known, however, probability distributions can describe these events on average. For a given incident particle, a random number is used to sample the probability distribution of interaction of that particle within the medium. If an interaction occurs, other random numbers are used to determine the interaction type, energy loss and change in direction of the incident particle. Any secondary

particles created in the interaction are also tracked using the same process. As these particles traverse a predefined region of interest, energy deposited within volumetric bins is recorded to produce a three dimensional dose distribution. This process is termed dose scoring. Monte Carlo simulation leads to very accurate results as long as the underlying physics that determine the probability distributions are well known in all particle energy ranges of interest.

4.2 EGSnrc and the BEAM code system

The most common Monte Carlo code for medical physics applications is based upon the Electron Gamma Shower (EGS) code developed initially by Nelson and Ford³. The early code was used at the Stanford Linear Accelerator Center to aid in experimental analysis and shielding design. Many subsequent versions of the code have been implemented with improvements in the accuracy and the ability to model increasingly complex geometries. The current version of the EGS code is maintained by the Ionizing Radiation Standards branch of the National research Council of Canada.

The BEAM code system represents a general purpose user code based on the EGSnrc project and was first released in 1995 by Rogers *et al*⁴. This user code was specifically written to aid in the modeling of therapy sources that were time consuming under the current EGSnrc code. BEAM is divided into separate graphical user codes that perform specific tasks in the simulation process and include BEAMnrc, DOSXYZnrc and BEAMDP.

BEAMnrc allows the easy construction of a radiotherapy accelerator through the use of several pre-coded accelerator components called component modules (CM). Each component module has its own set of input parameters that allow changes to its position, composition and geometry. Component modules also allow the tracking of particles histories or interactions using the latch bit option. Each CM can be associated with a latch number that is then recorded in the main output file. Several general input parameters exist that allow the user to define

various input and output options including the radiation source type, number of incident particles, output phase space parameters etc.

The output from BEAMnrc represents a record of all particles that cross a plane of user defined position and dimension. This record is termed the phase space and for a given particle contains information about its charge, energy, weight, direction and history. Particle information is written in the following order⁵

- Latch** Used to track the particles history of creation and interaction. Also specifies the charge of the particle
- E** Specifies the total energy of the particle
- X** is the X-position in cm
- Y** is the Y-position in cm
- U** is the X-direction cosine
- V** is the Y-direction cosine
- WT** is the particles weight

One important input component to all Monte Carlo simulation programs is the PEGS file. This file contains all cross sectional and stopping power data for all materials and particle energies contained within the simulation.

DOSXYZ represents a dose scoring system that is capable of using a previously generated phase space as an input. It tracks each particle from the phase space through a volume of user defined dimensions and composition or data from a CT set.

BEAMDP allows the user to extract useful information from phase spaces generated in BEAMnrc. It allows the choice of various types of analysis including:

(1) Fluence (and Energy fluence) vs. position, (2) Spectral distributions and (3) mean energy distributions.

4.3 Improving efficiency in Monte Carlo simulations

Variance reduction techniques offer ways to improve the computational efficiency of a simulation thereby reducing the time required to achieve a certain level of statistical variance or to reduce the statistical variance for a given simulation time. The techniques include:

Cut-off energies: Significant amounts of computational time can be spent tracking particles of relatively low energies with possibly little impact on the dose accuracy within a medium. By selecting a minimum energy in which particle transport is performed, relatively low energy particles will have their histories terminated at that threshold and the dose is deposited within the local voxel or component module. For photons and electrons, the cut-off energies are referred to as PCUT and ECUT respectively. The choice of these values depends upon the energy range of interest. For megavoltage therapy application, the choice of PCUT and ECUT is typically 0.01 MeV and 0.700 MeV respectively.

Range rejection: When range rejection is used, the range of the particle is calculated and compared to the distance of the closest region boundary. If the particle can't escape its current region with a total energy greater or equal to ECUT then the particles history is terminated and the dose is deposited at its current location.

Bremsstrahlung splitting: For simulations of x-ray beam production in radiotherapy accelerators, most of the computational time is spent tracking electron interactions as they generally undergo many more interactions per particle than photons. Bremsstrahlung splitting represents a variance reduction technique that creates N photons of weight of $1/N$ for each bremsstrahlung interaction. The three types of bremsstrahlung splitting available in the BEAMnrc

code are uniform (UBS), selective (SBS) and directional splitting (DBS). SBS and DBS have been used in this work and will be discussed in detail below.

In Selective Bremsstrahlung Splitting (SBS), the number of photons produced is dependent upon the direction of the parent charged particle and lies between a minimum and maximum splitting number. Charged particles that are directed at the phase space plane have higher splitting numbers and particles directed away from the phase space plane have lower splitting numbers. Each split photon is assigned a weight of $1/N$ to conserve energy. Efficiency can be improved by a factor of approximately 20 with SBS as compared to no variance reduction techniques⁵.

A second and more efficient method of variance reduction is directional bremsstrahlung splitting (DBS). DBS splits photons N times and assigns each a weight of $1/N$ as in SBS, but then determines whether the photon is incident upon the scoring plane. If so, it is left as is. Photons which are not incident upon the scoring plane are subject to Russian roulette to determine whether they are to be discarded. Elimination of photons not directed towards the scoring plane results in a great increase in efficiency as it eliminates the computation required to track these photons which have a low probability of contributing to the dose in the scoring plane. DBS has been shown to increase efficiency up to 8 times that of SBS⁵.

4.4 References

1. J. Cygler, G. Daskalov, G. Chan and G. Ding, "Evaluation of the first commercial Monte Carlo dose calculation engine for electron beam treatment planning," *Med. Phys.* **31**, 142-153 (2004).
2. E. Heath and J. Seuntjens, "Dosimetric evaluation of the clinical implementation of the first commercial IMRT Monte Carlo treatment planning system at 6 MV," *Med. Phys.* **31**, 2771-2779 (2004).
3. D. W. O. Rogers, "Fifty years of Monte Carlo simulations for medical physics," *Phys Med Biol* **51**, R287-301 (2006).
4. D. W. O. Rogers, B. A. Faddegon, G. X. Ding, C. M. Ma, J. We and T. R. Mackie, "BEAM: a Monte Carlo code to simulate radiotherapy treatment units," *Med. Phys.* **22**, 503-524 (1995).
5. D. W. O. Rogers, B. Walters and I. Kawrakow, Report No. PIRS-0509(A)revK, 2006.

Chapter 5

MATERIALS AND METHODS

5.1 INTRODUCTION.....	37
5.2 LOW QUALITY BEAM PRODUCTION	38
5.2.1 <i>Choice of low-Z targets</i>	38
5.2.2 <i>Target placement and primary-electron filter</i>	39
5.2.3 <i>Operation of the accelerator in the experimental imaging mode</i>	40
5.3 EXPERIMENTAL PLANAR IMAGING	41
5.3.1 <i>QC3 phantom</i>	41
5.3.2 <i>Image acquisition with the aS1000 electronic portal imager</i>	42
5.3.3 <i>Experimental image analysis</i>	44
5.4 MONTE CARLO MODEL AND SIMULATIONS	46
5.4.1 <i>Accelerator model</i>	46
5.4.2 <i>Model of spatial resolution phantom</i>	48
5.4.3 <i>Quantifying spatial resolution from generated phase spaces</i>	49
5.4.4 <i>Simulated investigation of photon focal spot size for various target combinations.....</i>	50
5.5 TRACKING THE SOURCE OF PHOTONS	52
5.5.1 <i>Resolution improvement in moving the external target into the target arm</i>	53
5.6 SPATIAL RESOLUTION ASSESSMENT IN CONE-BEAM CT.....	53
5.6.1 <i>Image acquisition, reconstruction and analysis.....</i>	54
5.7 REFERENCES	57

5.1 Introduction

The method of experimental beam production using a modern medical linear accelerator is presented. In order to investigate the optimal target design from a spatial resolution point of view, several different target parameters are designed and installed experimentally into the head of the accelerator. The different equipment modifications are presented as well as the general operating procedure of the accelerator in the low z imaging mode.

In order to quantify differences in spatial resolution between the various custom targets, a line pair phantom is used in conjunction with an electronic portal imaging device. The image acquisition and analysis is introduced.

Monte Carlo investigations prove to be an invaluable tool in to aid in the analysis of experimental results. Simulations were designed to study the trends in spatial resolution between the different targets and compare them to experimental results. Simulations were also designed to further investigate results that would otherwise be difficult to measure experimentally.

5.2 Low quality beam production

In this investigation, a dual energy Varian 2100EX (Varian Medical, Inc.) linear accelerator was used to produce experimental imaging beams. The accelerator is currently in clinical use at the Nova Scotia Cancer Center in Halifax, Nova Scotia, Canada. It is capable of producing a 6 MV and 18 MV treatment/imaging beams as well as electron beams of 4, 6, 9, 12 and 16 MeV.

5.2.1 Choice of low-Z targets

The choice of low-Z target material was based upon two main requirements: i) ease of procurement and machining to a required tolerance and ii) a sufficient density to allow full thickness targets to fit within the confined space of the linac head. Beryllium (Be, $Z = 4$), aluminum (Al, $Z = 13$) and tungsten (W, $Z = 74$) were obtained as disks measuring 50 mm in diameter and varying thicknesses dependent upon the continuous slowing down approximation range (R_{CSDA}) of electrons in that target material for a given energy. Henceforth, the target thickness as a percentage of the CSDA range for a given target material and electron energy will be termed $R_{\% \text{CSDA}}$. Three thicknesses were chosen for each material and incident electron energy combination to give $R_{\% \text{CSDA}}$ values of 20%, 60% and 100%. Actual target thicknesses are given in Table 5.1. For Monte Carlo simulations, a greater number of target thicknesses were used to give six $R_{\% \text{CSDA}}$ values between 10% and 100%.

Table 5.1: Actual thicknesses of the external targets in mm.

$R_{\%CSDA}$ (%)	Be			Al			W		
	20	60	100	20	60	100	20	60	100
4.5 MeV	3.0	10.0	15.0	2.1	6.2	10.4	0.38	1.01	1.82
7.0 MeV	5.1	15.0	25.0	3.1	9.4	15.7	0.52	1.53	2.52

5.2.2 Target placement and primary-electron filter

Experimental targets were installed into unused ports in the carousel of a Varian 2100EX accelerator (Varian Medical Inc.) using custom made collars similar to those normally used to hold the electron scattering foils. This process is shown in Figure 5.1 (a). To access the carousel, it is necessary to remove all covers on the accelerator head as well as one shielding block. To gain access to the desired port, the carousel is switched to manual mode by way of a threeway switch located within the gantry stand. The carousel position is controlled by a rotary dial located on the same board. The collar assembly was machined in house from aluminum and can be seen in Figure 5.1 (b). Each collar holds a target such that the upstream surface was positioned at a fixed distance of 9 mm from the bottom surface of the beryllium exit window. This separation is the minimum gap that could be achieved without risk of collision with internal components as the carousel rotates.

Since targets with $R_{\%CSDA}$ values as low as 10% were used, an electron filter was required in order to remove the remaining primary electrons. Polystyrene was chosen as the filter material due to its high stopping power and low x-ray efficiency relative to higher Z materials for the electron energies of interest. The filter was held in position in the upper accessory tray. Monte Carlo simulations were conducted using the accelerator model discussed in section 5.4.1 to

determine the minimum thickness required. The electron energy spectrum was analysed at isocenter for increasing filter thicknesses to determine when the residual peak produced from the primary electrons disappeared. It was found that all primary electrons were stopped with 3.29 cm of polystyrene. This thickness was used for all targets in an effort to keep scatter conditions relatively constant.

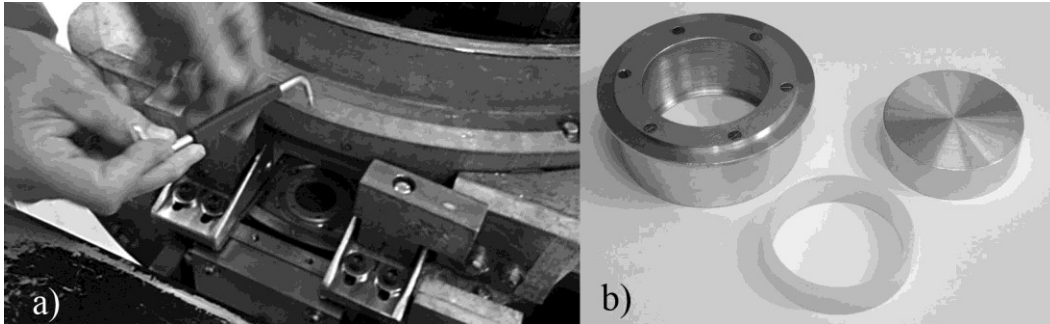


Figure 5.1: (a) Installation of the custom targets into the carousel of the accelerator head. (b) The machined collar with an aluminum target and nylon sleeve used to hold the target at the correct position.

5.2.3 Operation of the accelerator in the experimental imaging mode

In order to generate the experimental beams, the linac was operated in electron mode. A schematic comparison between the clinical imaging beam line and the experimental imaging beam line is seen in Figure 5.2. In electron mode, the clinical target is retracted and the electron pencil beam is allowed to continue down through the primary collimator and out the exit window. The position of the carousel was controlled manually, as discussed in section 5.2.2, to position the desired target into the beam line. Due to the use of thin targets, the ion chamber is exposed to a photon beam as well as primary electrons. The beam monitoring system recognises that the beam is operating outside of normal parameters and trips various interlocks designed to halt the beam. Also, systems monitoring the position of the carousel detect an error and exert an interlock. In order to operate the accelerator, it was necessary to override the following interlocks: DS12, UDRS, UDR1, UDR2, DPSN, COLL, ACC, CARR and FOIL.

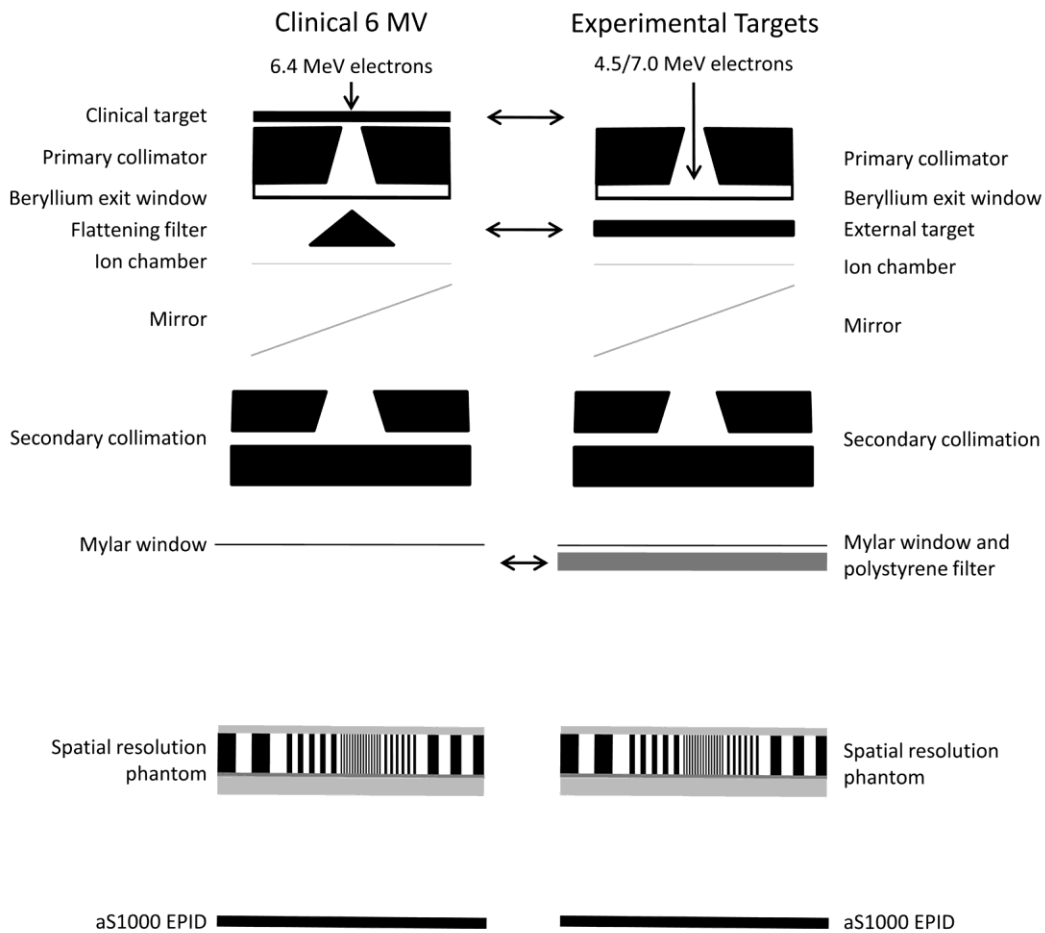


Figure 5.2: A block diagram illustrating the differences in the generation of the clinical 6 MV beam (left) and the experimental imaging beam (right).

5.3 Experimental planar imaging

5.3.1 QC3 phantom

The QC3¹ (SeeDOS Ltd., Bedfordshire, UK) was chosen as an appropriate phantom to derive the modulation transfer function (MTF) due to its simplicity and suitability for MV imaging applications. It contains line pair regions of 0.1, 0.2, 0.25, 0.4, and 0.75 line pairs per mm that consist of alternating bars of lead (11.34 g cm^{-3}) and Delrin (1.42 g cm^{-3}). The phantom was positioned at isocenter (its surface approximately 99 cm from the therapy source) using a Styrofoam jig that held it rotated 45 degrees in the axial plane to avoid aliasing of the bar

patterns². The phantom and its corresponding contrast and spatial resolutions are represented in Figure 5.3.

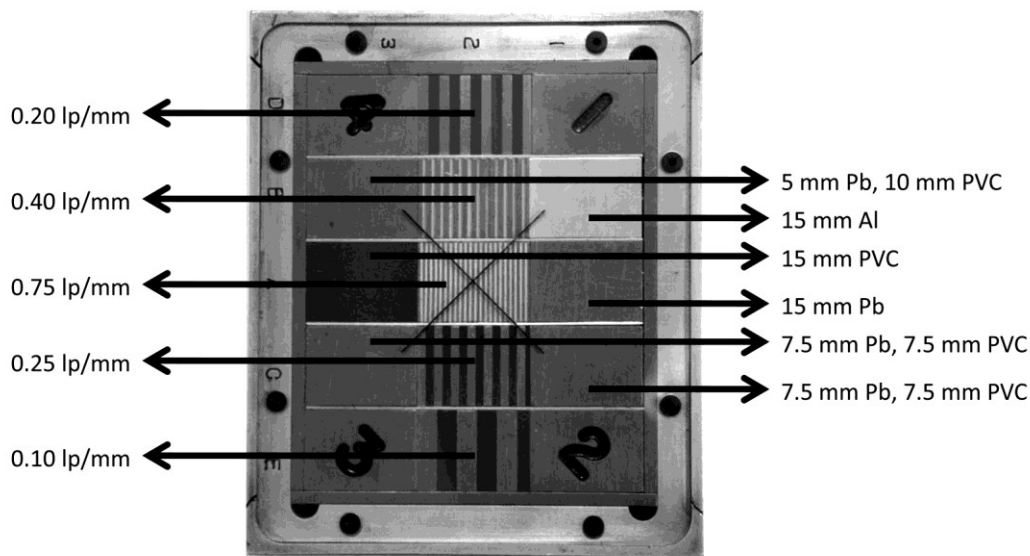


Figure 5.3: The different contrast and spatial resolution regions of the QC3 phantom are shown.

5.3.2 Image acquisition with the aS1000 electronic portal imager

A Varian aS1000/IAS3 (Varian Medical Inc.) imaging system was used for all image acquisition experiments. The IDU20 EPID was positioned 130 cm from the therapy target as it represents a typical source to imager distance (SID) used in portal imaging as well as in cone-beam CT. The panel was held in place by a custom made jig that was capable of adjusting the tilt of the imaging panel such that its surface is positioned perpendicular to the central axis of the imaging beam. The jig was secured to the treatment couch using a fixation bar that is normally used in relocating patient immobilization systems. Figure 5.4 shows the experimental setup including the aS1000 in its base, as well as the QC3 phantom. The 4 MeV electron mode was reserved as an experimental beam and was not in clinical use at the time of this research. In order to access this mode, it was required to insert a separate carousel bending magnet board and program board

that were previously tuned to produce a clinically acceptable 4 MeV electron beam.

Once the custom targets are installed and positioned in the beamline, the gantry is rotated to 90 degrees and the imager is centered on the central axis. The 3.29 cm polystyrene filter is then inserted into the upper accessory tray. The jaws were set to 14 x 14 cm² for all QC3 images. The IDU20 imager is connected to a digitization unit, which is in turn connected to the accelerator control console as well as the research dedicated IAS3 workstation via cables routed out of the bunker through the cable duct. Before operation of the accelerator in low-Z target mode is possible, the appropriate interlocks are overridden and either the 4 MeV or 6 MeV electron mode is selected depending on the desired incident electron energy. Repetition rates were set to 1000 MU/min for all experimental beams. This setting partially compensated for the approximate three orders of magnitude drop in the beam current while operating in electron mode as compared to photon mode. Image acquisition was controlled using the manufacturer supplied software, AMaintenance (Varian Medical, Inc.). This software controlled the imaging process through a graphical user interface called the IAS3 service monitor. The detector acquisition mode was set to "synchronized to beam pulses" for all exposures. Image exposure was controlled by setting the number of beam pulses per frame and was held roughly constant between targets by comparing pixel values for a given region in the phantom. The number of beam pulses per frame was selectable between 1 and 4095. Utilizing beam pulses as opposed to cMU (chamber monitor unit) pulses was necessary to avoid the wide range of dose per MU values for the different targets that caused either too long (imager timeout at 30 seconds) or too short (low imager exposure) exposure times. Images were integrated between 2000 to 4095 beam pulses per frame (which corresponds to approximately 20 to 30 seconds per frame), depending upon the thickness of target, to give a sufficiently high signal at the detector to reduce pixel quantization errors and increase signal

to noise. A more complete set of imaging parameters is outlined in Appendix A. Prior to imaging, dark current and flood field corrections were applied using acquisition software supplied by the manufacturer. The flood field correction was able to correct for the forward peaked beam profiles due to the absence of a flattening filter. It also corrected for individual variations in pixel sensitivity. Frame averaging was set to 30 for the dark field images and flood field images were averaged 10 times. Acquired images of the QC3 phantom were averaged three times each.

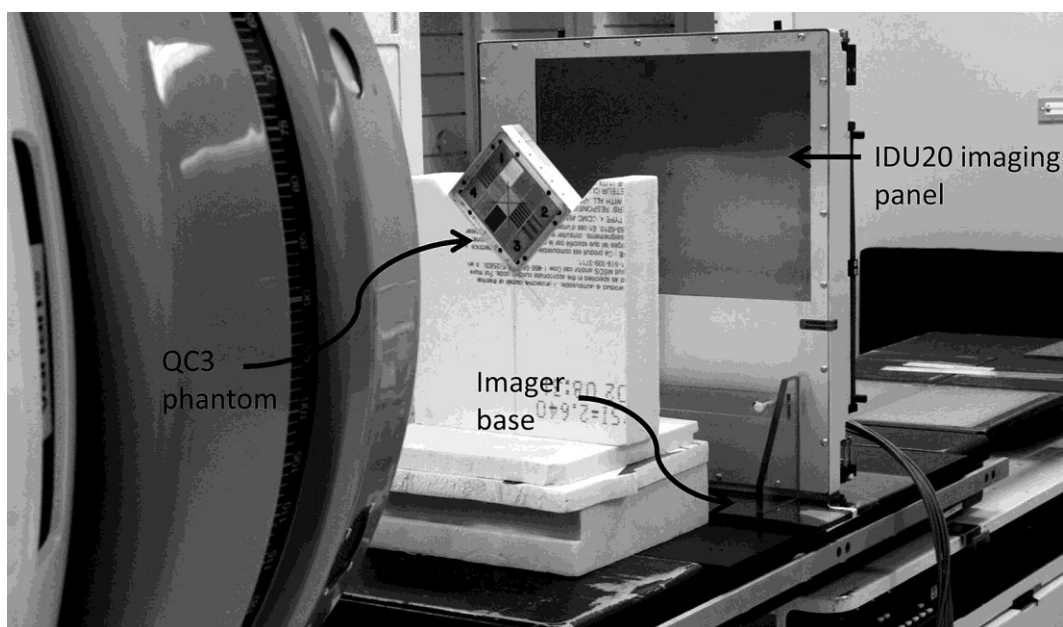


Figure 5.4: The experimental setup for planar imaging is shown, including the IDU20 panel, the imager base and the QC3 phantom.

5.3.3 Experimental image analysis

The MTF can be accurately determined by analysing a line spread function or step function. However, due to the precision required and difficulty in aligning the collimation with the beam axis, this method was not deemed practical for this investigation. A square wave of frequency f can be represented by the sum sinusoidal waves of frequency of f , $3f$, $5f$ and so on. Coltman³ has shown that the MTF of cyclic bar patterns can be represented as

$$MTF(f) = \frac{\pi}{4A_0} \left(A(f) + \frac{A(3f)}{3} - \frac{A(5f)}{5} + \frac{A(7f)}{7} \dots \right) \quad (5.1.)$$

where A and A_0 are the output and input amplitudes respectively and f is the spatial frequency of the square wave bar pattern. Consider a cutoff frequency f_c where the MTF drops to and stays at zero. Providing that the bar pattern frequency f is above $f_c/3$, then equation 5.1 can be written as

$$MTF(f) = \frac{\pi A(f)}{4 A_0}, \quad f \geq \frac{f_c}{3} \quad (5.2.)$$

Since a square wave of frequency f can be constructed from the sum of sinusoidal waves with frequencies with odd multiples of f for frequencies of $f_c > f \geq f_c/3$, a square wave input will result in a sinusoidal output due to the exclusion of higher order terms. In the literature⁴, the standard deviation of a line pair region is termed the modulation (M) to avoid confusion with the traditional use of taking the standard deviation of a uniform region. Since the standard deviation of an input square wave is equal to its amplitude ($M_0 = A_0$) and the amplitude of the output sinusoidal wave can be related to the standard deviation by $M\sqrt{2} = A$, the preceding substitutions yield

$$MTF(f) = \frac{\pi\sqrt{2} M(f)}{4 M_0}, \quad f \geq \frac{f_c}{3} \quad (5.3.)$$

As it was not necessary to calculate the absolute MTF, we opted to follow the method proposed by Rajapakshe et al² in which the MTF at frequency f was normalized to the MTF of the lowest frequency line pair region f_1 . This allows us to write our main equation for the relative MTF (RMTF) as

$$RMTF(f) = \frac{M(f)}{M(f_1)} \quad (5.4.)$$

$M(f)$ represents the output modulation of the line pair region of interest and $M(f_1)$ is the output modulation of the lowest frequency line pair region. Due to difficulties in extracting the modulation from a noisy image, Droege and Morin⁴

have suggested a method of using the pixel variance of a given line pair region to determine $M(f)$ and $M(f_1)$ as seen below.

$$M^2(f) = \sigma_m^2(f) - \sigma_n^2(f) \quad (5.5.)$$

Where $\sigma_m^2(f)$ represents the variance of a given line pair region and $\sigma_n^2(f)$ represents the variance due to random noise in the image. To obtain the random noise, two sequential images are subtracted and the variance is calculated from the difference. This has the advantage of removing the variance due to non-noise related variations in the image and only leaves the contribution from random noise. As outlined by Rajapakshe *et al*², the variance of the subtracted region of interest will be

$$\sigma_{sub}^2 = \sigma_1^2 + \sigma_2^2 \quad (5.6.)$$

Since the variances of two sequential images are assumed to be equal, it follows that the variance due to random noise of any one image (σ_n^2) should be equal to

$$\sigma_n^2 = \frac{\sigma_{sub}^2}{2} \quad (5.7.)$$

Relative MTF curves for the various target combinations were compared by determining the spatial frequency (f_{50}) at which the RMTF dropped to 50% of its maximum value.

5.4 Monte Carlo model and simulations

5.4.1 Accelerator model

A previously validated model of a Varian 2100EX linear accelerator⁵ constructed using the EGSnrc/BEAMnrc Monte Carlo package⁶ was used in this investigation. A complete list of component modules is contained within the EGS input file represented in Appendix B. Simulation parameters were adjusted to match the experimental linac configuration outlined in section 5.2. All simulations involving the spatial resolution phantom had jaw settings of 16 x 16 cm². This differed

from the 14 x 14 cm² field size used in the experimental acquisition, however, it was found that the change in jaw setting did not produce a statistically significant change in f_{50} , but did reduce the simulation time as less particle interactions needed to be calculated within the jaw material that would have been present in providing the further collimation of the 14 x 14 cm² field from the 16 x 16 cm² field.

Incident electrons were assumed to be symmetric and Gaussian in spatial distribution⁷. Their initial kinetic energy was determined to be 7.0 MeV and 4.5 MeV for the nominally 6 MeV and 4 MeV beams respectively⁸.

The FWHM values of the incident 4.5 and 7.0 MeV electron beams were measured by placing low sensitivity MD-55 Gafchromic film (2-100 Gy) into the carousel at the front surface of the custom target collar with the target removed at the time of irradiation. Calibration exposures were taken and all film was scanned with a transmission based film scanner. This allowed for the construction of a dosimetric curve in which the removal of nonlinearities inherent in the film and digitization process could be removed. Profiles were taken across the irradiated film regions and fitted with a Gaussian curve within MATLAB (Mathworks, Natick MA). Using Monte Carlo methods, it was possible to determine the percentage increase in the FWHM of the incident electron beam as it traveled through the primary collimator exit window and the air gap. The results of this investigation are examined in section 6.2. The FWHM of the incident electron beam in vacuum was determined to be approximately 2 mm for the 6 MeV electron mode and this was then used as an input parameter in all subsequent simulations to maintain consistency. The actual results of the width of the incident electron beam are only of use in the analysis of the experimental MTF curves produced by the various targets.

Directional bremsstrahlung splitting (DBS) was used with a splitting field radius of 20 cm at 100 cm and a splitting number of 1000. Since no flattening filter was present, electron splitting was conducted at the bottom surface of the

polystyrene filter. The Russian roulette plane was located within the polystyrene filter 2.6 cm above the splitting plane.

A 26 layer model of a Varian aS500 imaging panel existed upon the commencement of this research. This detector model was previously used for contrast measurements and was tested for its suitability in spatial resolution. The modeled panel was compared to its real world counterpart and it was found that it was not possible to easily match the spatial resolution performance of the imagers, so alternate methods of quantifying modulation were explored. The phase space was placed 30 cm beyond isocenter in place of the aS1000 EPID. For all simulations, the global electron and photon cut-off energies (ECUT and PCUT) were set to 0.7 MeV and 0.01 MeV respectively.

All simulations were run on a dedicated distributed computing cluster managed by the Sun Grid Engine (Sun Microsystems, Santa Clara, US). The cluster consisted of a control unit and 24 cores in 14 nodes. Jobs would be distributed by the grid engine to the various cores and phase space data would be calculated and sent back to the control for storage on a high capacity drive.

5.4.2 Model of spatial resolution phantom

A spatial resolution phantom similar to the line-pair section in the QC3 phantom was modeled for this investigation. The VARMLC component module was used to create 1.5 cm thick alternating regions of lead and Delrin similar to those found in the QC3 phantom. A full parameter list of phantom parameters is shown in Appendix B between lines 160-215. Since the aS1000 imager was not modeled, its degradation to the total MTF was not present and higher frequency line pairs were added to enable the sampled modulation values to cover a broader range of the MTF curve. A total of five divergent line pair regions between 0.2 and 1.17 line pairs/mm were modeled as compared to the five frequencies between 0.1 and 0.75 line pairs/mm as found in the QC3 phantom. A 3 mm layer of PMMA was added to the front side of the line pair regions and 2 mm of aluminum

followed by 17.9 mm of PMMA were added to the back side such that the modeled and experimental phantoms would be radiologically equivalent. The front of the complete modeled phantom was placed at an SSD of 99 cm which was consistent with the placement of the QC3 at isocenter.

5.4.3 Quantifying spatial resolution from generated phase spaces

Phase space files of 12 GB for each target were captured which made it computationally intensive to perform the two dimensional binning required to take advantage of the analysis method involving the variance as proposed by Rajapakse *et al*². It was therefore decided to use the fluence modulation to calculate the relative MTF (RMTF). Fluence vs. position profiles were first acquired across all line pair regions using BEAMdp⁹. 450 bins between ± 1.5 cm were used to score photons along the axis (y) containing the variations in fluence from the line pair regions. Bin sizes in the x dimension were 7 cm in order to achieve better statistics. An example fluence vs position profile extracted from the phase space created using the 60% thickness aluminum target with 7.0 MeV incident electrons is seen plotted in Figure 5.5. Error bars are not included for the sake of clarity; however, the standard deviation is below 1%.

Modulation was extracted from these plots using the following method

$$M(f) = \frac{\varphi_{max}(f) - \varphi_{min}(f)}{\varphi_{max}(f) + \varphi_{min}(f)} \quad (5.8.)$$

where φ represents the fluence within the line pair region of interest. The RMTF is calculated as in equation 5.4.

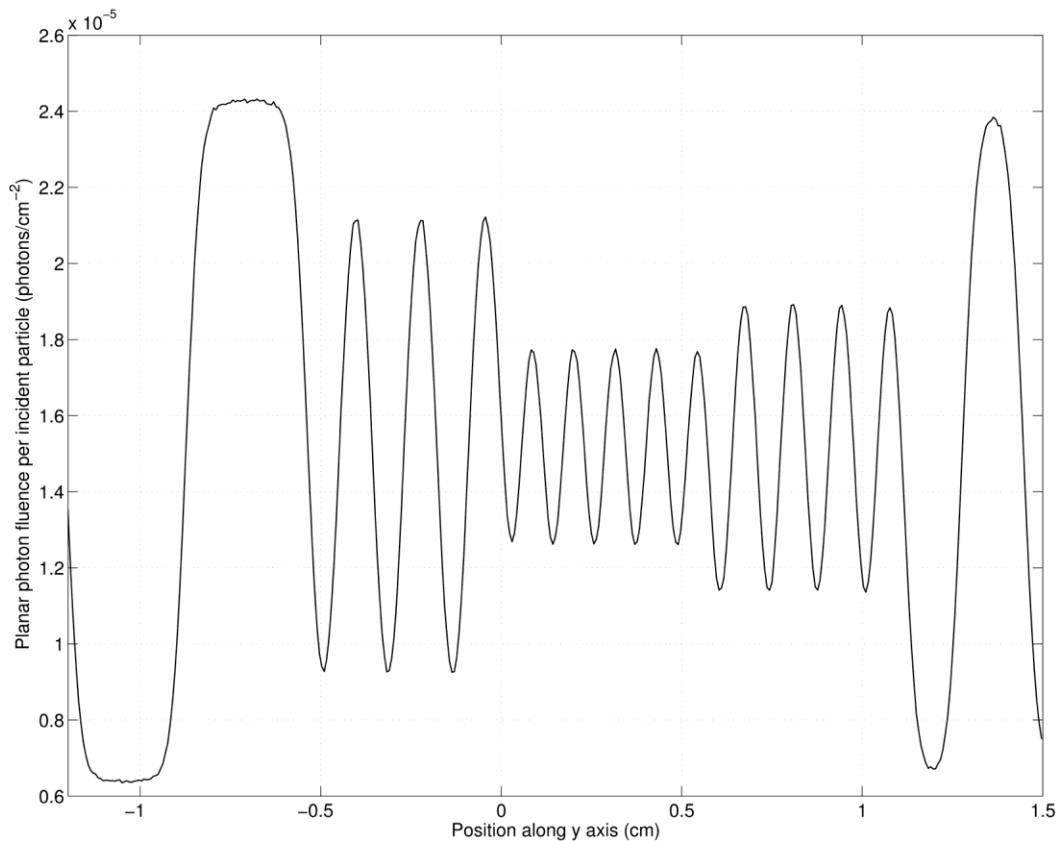


Figure 5.5: A typical fluence vs. position plot calculated from the phase using BEAMDP.

5.4.4 Simulated investigation of photon focal spot size for various target combinations

It was of interest to investigate the change in photon focal spot size for the various targets as the focal spot size is an important factor in determining the spatial resolution. Simulations were run in which a 2 mm Gaussian electron beam was incident upon the various external targets placed 9 mm from the vacuum window. A phase space was recorded at the lower surface of each target. Selective bremsstrahlung splitting was used with splitting numbers between 100 and 1000 and a splitting field size of 15 cm at 10 cm (the approximate location of the phase space). Simulations were run until approximately 60 million particles were scored for each phase space. To determine the size of the focal spot, a method of collimation similar to that used

by Jaffray *et al*¹⁰ was used. In Jaffray's work, slit-collimators were used in conjunction with a CdTe diode and CT reconstruction techniques to compute the size of the focal spot. The collimation device was placed on a translation stage which was held on a rotation stage. The diode was held stationary at the bottom of the collimation device as the whole assembly was translated across the central axis. At each position, the diode would be exposed to a different strip across the focal spot and its signal would represent the integrated dose from each point along that strip. The process was then repeated for multiple rotation angles. The final data were then reconstructed to provide the 2 dimensional shape of the focal spot. This method of collimation was replicated virtually by examining each particle in the phase space and rejecting those beyond some critical angle. This effectively allowed the rejection of those photons whose direction was not roughly parallel to the central axis. Using MATLAB, photons of angles greater than one degree were rejected and the distance from the central axis of the remaining photons was calculated and binned to produce a fluence vs. radial position plot. One degree was chosen as a rejection angle as it was small enough that photon divergence effects were negligible (the phase space was located at the bottom of the target and different target thickness caused this position to vary). Also, one degree was large enough that a sufficiently large number of photons from the phase space would not be rejected. The fluence for each circular bin was normalized to its area.

Since the electron beam is known to scatter and broaden as it travels deeper into the target, it was of interest to determine the degree of broadening at various depths in the target for different target materials. It was hypothesized that this spreading of electrons would be responsible for a broadening of the photon focal spot in thicker targets. A simple simulation was set up with a 2 mm Gaussian electron beam incident upon a full thickness beryllium target and a full thickness tungsten target after passing through the 9 mm air gap and beryllium exit window. The targets were created using three SLABS component modules

which allowed the simultaneous placement of phase spaces within the target at depths of 0%, 40% and 80% of the $R_{\%CSDA}$ value. BEAMDP was then used to generate plots of electron fluence as a function of radial position.

Simulations were also designed to track the depth of photon creation in the target. Each target was constructed using a single SLABS component module and divided into 20 equally thick layers. Each layer was assigned a unique latch bit and the latch option was set to inherited latch (set by interactions). Since bits 24 to 28 recorded the region of creation of the secondary particle, it was possible to identify which layer of the target each photon was created in. MATLAB was used to analyse the $5 \times 5 \text{ cm}^2$ phase spaces located at isocenter and create a frequency distribution of the number of photons created in each layer of the target. This simulation was run for the 4.5 MeV/Al, 7.0 MeV/Be, 7.0 MeV/Al and 7.0 MeV/W targets.

5.5 Tracking the source of photons

Previously, Roberts *et al*¹¹ commented on the high fraction of bremsstrahlung photons created within the primary collimator exit windows of some linac models used by various authors experimenting with low Z-external targets. They noted that all investigators reported high resolution images despite large air gaps between the primary collimator and low-Z target. In particular, Flampouri *et al*¹² achieved high resolution images despite a 15 cm air gap which resulted in an 8 cm wide electron beam at the level of the target. Roberts *et al* went on to show that for the accelerator used in Flampouri's case, the central $5 \times 5 \text{ cm}^2$ of a $20 \times 20 \text{ cm}^2$ field, 70.95% of the energy fluence arose from the electron window and 28.23% from the carbon target.

It was of interest to characterize the photon contribution from components within the accelerator other than the external targets. The modeled accelerator in this case was the same as in section 5.4.1 except with the spatial resolution phantom removed. The jaws were set to define a $20 \times 20 \text{ cm}^2$ field at isocenter

and latch bits were used to track the origin of all photons that crossed the inner 5 cm x 5 cm² region of a 24 x 24 cm² plane also located at isocenter. The latch option was set to inherited latch (set by interactions) and bremsstrahlung splitting was turned off. Both incident electron energies were investigated as well as all three target materials for target thickness of 10% and 100%. Approximately 3.5 million particles were collected in each phase space.

5.5.1 Resolution improvement in moving the external target into the target arm

It is known that the focal spot size in conjunction with its distance to the object and detector play an important role in defining the spatial resolution of a system. By placing the target outside of the vacuum system and at the location of the carousel, it is not only exposed to a wider electron beam, but it's also placed closer to the object and detector which presents a geometric disadvantage in terms of spatial resolution for finite focal spot sizes. It was of interest to investigate any improvement in spatial resolution by moving the custom target from the carousel to the usual location within the target arm, contained in vacuum. Simulations were run with the same parameters as in section 5.4.1, but now the target material in the carousel was switched to air and an aluminum target was placed at the location of the target arm. Simulations were run with both 4.5 and 7.0 MeV incident electrons for the 60% thickness target. A phase space was captured 130 cm from the therapy source and an MTF was calculated as per section 5.4.3.

5.6 Spatial resolution assessment in cone-beam CT

Faddegon *et al*¹³ have investigated spatial resolution in MV CBCT using an unflattened 4 MV beam produced in a Carbon target installed in a Siemens Primus linac (Siemens Medical Systems, Malvern, US). They found a factor of 2 increase in spatial resolution between the treatment beam line and imaging beam line. The final phase of this research aims to use select targets from the

planar imaging investigation to compare acquired CBCT sets acquired in the imaging and treatment modes.

5.6.1 Image acquisition, reconstruction and analysis

Cone-beam images were acquired similarly to the planar images as described in section 5.3.2. Each projection was acquired with the gantry positioned at 90 degrees and the imager resting on the couch. The QC3 phantom was replaced by the CATphan CT imaging phantom (The Phantom Laboratory Inc., Salem, US) which was held on top of a rotation stage attached to a stepping motor. The stepping motor was mounted on a base which allowed fine adjustments in its lateral position. In order to ensure the axis of rotation was aligned with the center of the detector to avoid blurring in the reconstructed image. The phantom was positioned at isocenter with the imager 130 cm from the therapy source. Figure 5.6 shows the experimental setup of the imaging panel with the CATphan phantom on top of its rotation stage.

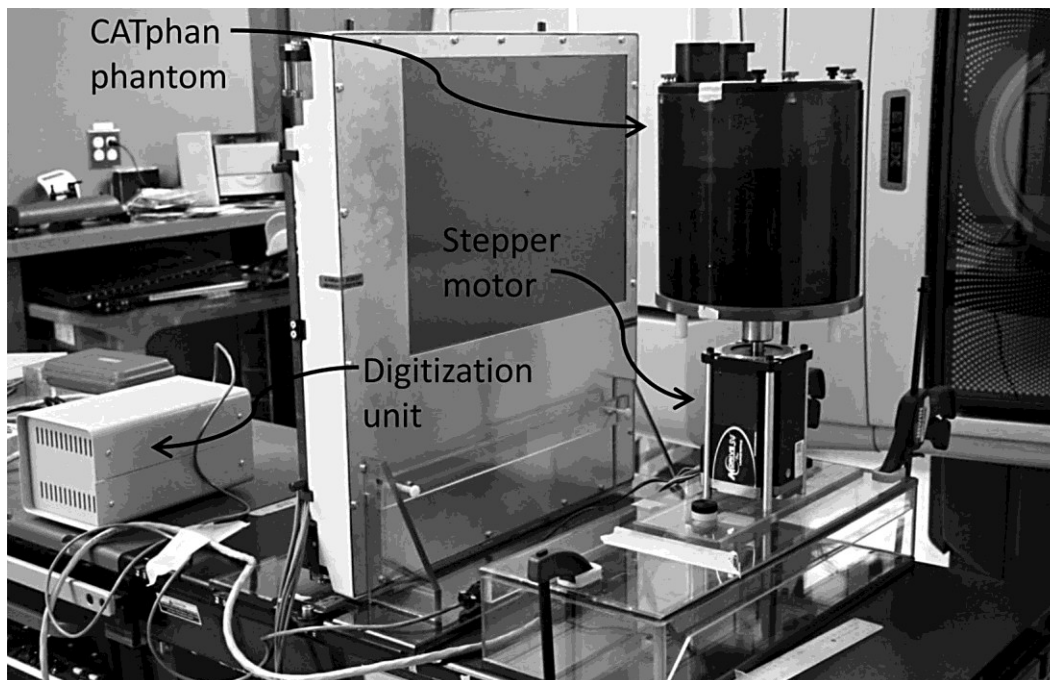


Figure 5.6: The experimental setup for cone-beam acquisition is shown including the CATphan phantom, stepping motor and digitization unit.

Two previously installed targets were compared to the clinical 6 MV beam: a 1.0 cm thick aluminum target with 7.0 MeV incident electrons (7.0 MeV/Al), and a 0.65 cm thick target with 3.5 MeV incident electrons (3.5 MeV/Al). Each target thickness represented approximately 60% of the R_{CSDA} for the given incident electron energy. The exposure for each image was determined by setting the number of cMU pulses per frame. cMU pulses represent the integrated signal collected in the ion chambers and differ from beam pulses, which were used in the planar imaging investigation. cMU pulses were chosen as they were previously related to dose for each target by other investigators¹⁴. This enabled the acquisition of CBCT sets with similar doses. Dose was related to cMU pulses by placing a solid water phantom of similar dimensions on the rotation stage and measuring the dose for a given number of cMU pulses using a calibrated ion chamber (PTW 31010, 0.125 cm³) placed at the phantom center. It was determined that the number of cMU pulses per frame should be set to 12, 524 and 1492 to deliver 20 cGy to the phantom center for the clinical 6 MV, 3.5 MeV/Al and 7.0 MeV/Al targets respectively.

To ensure that the reconstructed images would not be limited by noise, a high dose of 150 cGy per set was delivered to the center of the phantom. This required the use of 30, 1310 and 3730 cMU pulses per frame for the 6 MV, 3.5 MeV/Al and 7.0 MeV/Al beams respectively with three frame averages per image

The imaging sequence was performed in the following order:

1. The beam was turned on, but beam pulses were held off by the acquisition software via the gating interface until prompted by the user.
2. The first image was acquired with the IAS3 system integrating the signal over the predefined number of cMU pulses.

3. The beam was again held off by the acquisition software through the gating interface after the required number of cMU pulses had been delivered.
4. The rotation stage was rotated by a set amount (two degrees).
5. After a short delay to allow the stand to stabilize, the beam hold-off was removed and the next image was acquired.
6. Steps 3 to 5 were repeated to acquire the desired number of projections (180).

Acquired image sets were reconstructed using the Feldkamp-Davis-Kress (FDK) algorithm¹⁵ which has been previously implemented within a graphical user interface¹⁴ encoded within MATLAB. One millimeter axial slices were reconstructed for each of the three image sets.

The spatial resolution section of the CATphan phantom contained 21 regions of alternating aluminum and epoxy bars with spatial frequencies between 1 and 21 line pairs/cm. Analysis of the three cone-beam sets were done by visually identifying the highest frequency line pair region visible within the axis slice centered on the spatial resolution section.

5.7 References

1. R. Rajapakshe, T. J. Radcliffe and S. Shalev, "Quality control for on-line portal imaging systems," Proc. SPIE **1897**, 121-127 (1993).
2. R. Rajapakshe, K. Luchka and S. Shalev, "A quality control test for electronic portal imaging devices," Med. Phys. **23**, 1237-1244 (1996).
3. J. Coltman, "The Specification of Imaging Properties by Response to a Sine Wave Input," J. Opt. Soc. Am. **44**, 468-469 (1954).
4. R. T. Droege and R. L. Morin, "A practical method to measure the MTF of CT scanners," Med. Phys. **9**, 758-760 (1982).
5. E. J. Orton and J. L. Robar, "Megavoltage image contrast with low-atomic number target materials and amorphous silicon electric portal imagers," Phys. Med. Biol. **54**, 1275-1289 (2009).
6. D. W. O. Rogers, B. A. Faddegon, G. X. Ding, C. M. Ma, J. We and T. R. Mackie, "BEAM: a Monte Carlo code to simulate radiotherapy treatment units," Med. Phys. **22**, 503-524 (1995).
7. C. Karzmark, C. Nunan and E. Tanabe, *Medical Electron Accelerators*. (McGraw-Hill, 1992).
8. J. L. Robar, "Generation and modeling of megavoltage photon beams for contrast-enhanced radiation therapy," Phys. Med. Biol. **51**, 5487-5504 (2006).
9. C. M. Ma and D. W. O. Rogers, Report No. PIRS-0509(C)revA, 2007.
10. D. A. Jaffray, J. J. Battista, A. Fenster and P. Munro, "X-ray sources of medical linear accelerators: Focal and extra-focal radiation," Med. Phys. **20**, 1417-1427 (1993).
11. D. A. Roberts, V. N. Hansen, A. C. Niven, M. G. Thompson, J. Seco and P. M. Evans, "A low Z linac and flat panel imager: comparison with the conventional imaging approach," Phys. Med. Biol. **53**, 6305-6319 (2008).
12. S. Flampouri, P. M. Evans, F. Verhaegen, A. E. Nahum, E. Spezi and M. Partridge, "Optimization of accelerator target and detector for portal imaging using Monte Carlo simulation and experiment," Phys. Med. Biol. **47**, 3331-3349 (2002).
13. B. A. Faddegon, V. Wu and J. Pouliot, "Low dose megavoltage cone beam computed tomography with and unflattened 4 MV beam from a carbon target," Med. Phys. **35**, 5777-5786 (2008).
14. J. L. Robar, T. Connell, W. Huang and R. Kelly, "Megavoltage planar and cone-beam imaging with aluminum linear accelerator targets: dependence of image quality improvement on beam energy and patient separation," (2009).
15. L. A. Feldkemp, L. C. Davis and J. W. Kress, "Practical cone-beam algorithm," J. Opt. Soc. Am. **1**, 612-619 (1984).

Chapter 6

RESULTS AND DISCUSSION

6.1	INTRODUCTION.....	58
6.2	CHARACTERIZING THE INCIDENT ELECTRON BEAM	58
6.3	TRACKING THE SOURCE OF PHOTONS	61
6.4	SIMULATION OF FOCAL SPOT SIZE FOR VARIOUS TARGET PARAMETER COMBINATIONS	62
6.4.1	<i>Simulation of electron beam broadening</i>	<i>64</i>
6.4.2	<i>Simulation of depth of photon creation.....</i>	<i>65</i>
6.5	SIMULATED PHOTON FLUENCE FROM A MODELED LINE PAIR PHANTOM	66
6.6	EXPERIMENTAL DETERMINATION OF f_{50}.	68
6.7	RESOLUTION IMPROVEMENT IN MOVING THE LOW-Z TARGET INTO THE TARGET ARM .	72
6.8	SPATIAL RESOLUTION ASSESSMENT IN CONE-BEAM CT.....	73
6.9	CLINICAL IMPLEMENTATION OF A LOW-Z, EXTERNAL TARGET IMAGING MODE	74
6.10	REFERENCES.....	77

6.1 Introduction

In this chapter, experimental and Monte Carlo simulated results are presented. The suitability of the external targets for cone-beam CT is also discussed. Results of both planar and cone-beam studies produced with the low Z targets are compared to images acquired from beams produced with the clinical target.

6.2 Characterizing the incident electron beam

It was necessary to measure the incident electron beam width to enable a thorough comparison between the two energies in the experimental planar imaging study, as well as to provide an input parameter for the Monte Carlo investigation. Figure 6.1 (a) and (b) show the scanned film sections at the level of the external target for the 4.5 MeV and 7.0 MeV incident electron beams respectively. Both distributions show a slight asymmetry which is consistent with the results published by Jaffray *et al*¹ who reported asymmetric photon focal spots for energies of 6 MV and 18 MV on two Varian 2100C accelerators. Figure

6.1 (c) shows a typical dose profile and the fitted curve across the film region exposed to the incident 4.5 MeV electron beam. The FWHM values of the 4.5 MeV and 7.0 MeV electron beams at the level of the target were calculated to be 2.7 ± 0.2 mm and 2.3 ± 0.2 mm respectively. Uncertainty was calculated by taking 10 profiles at different angles and calculating the standard deviation of the results. The magnitude of the standard deviation in both energies is mostly attributed to the slightly elliptic shape of the dose distribution.

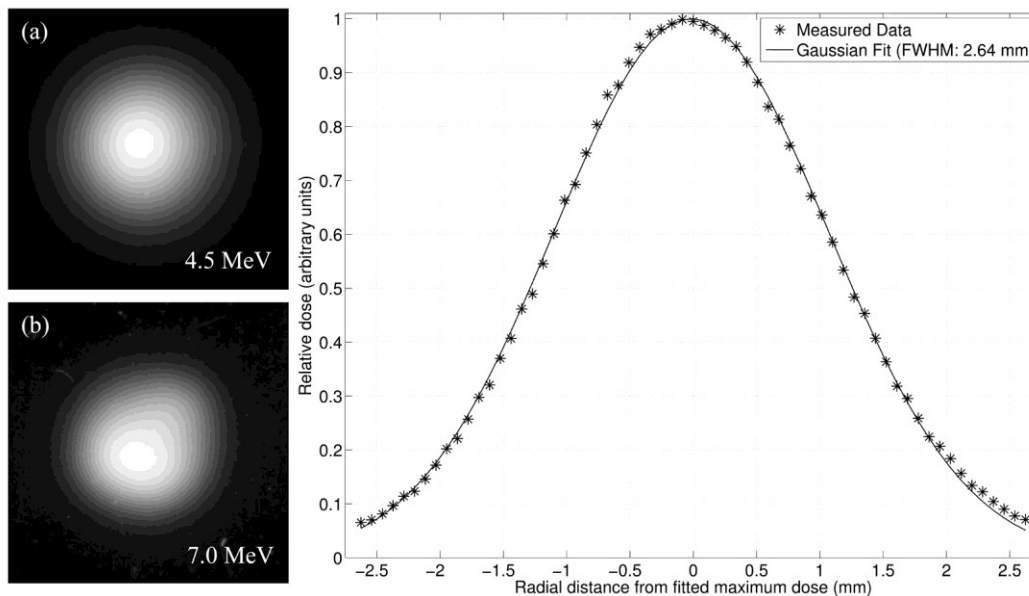


Figure 6.1: The digitized film regions at the upstream surface of the external target for the 4.5 MeV (a) and 7.0 MeV (b) incident electron beams respectively. (c) A typical dose profile across the film region exposed to the 4.5 MeV incident electron beam.

Monte Carlo simulations were created to model the degree of spreading due to scatter and the subsequent broadening of the electron beam as it traversed through the beryllium exit window and a 9 mm air gap. A modeled 2 mm Gaussian electron beam was set incident upon a slab of beryllium with the same thickness as the exit window and a 9 mm air gap. Phase spaces were concurrently placed at the front side of the beryllium slab and at the back side of

the air slab. The simulation was done for both the 4.5 MeV and 7.0 MeV beams and electron fluence vs. position plots were created within BEAMdp.

Figure 6.2 shows the electron fluence plotted as a function of radial distance from the central axis for the 4.5 and 7.0 MeV electron beams at the level of the external target. The electron fluence vs. radial position in vacuum is included for comparison. It was found that monoenergetic electron beams of 4.5 MeV and 7.0 MeV have a FWHM increase of 13.8% and 6.7% respectively before reaching the target surface. The greater spread of the 4.5 MeV beam is consistent with the fact that the mass angular scattering power is higher for lower energy electrons. To extrapolate the approximate size of the electron beam in vacuum, the calculated FWHM at the level of the target was divided by the determined percentage increase of 13.8% and 6.7% for the 4.5 MeV and 7.0 MeV beams respectively. In vacuum, the FWHM of the 4.5 MeV and 7 MeV beams were calculated to be 2.4 ± 0.1 mm and 2.1 ± 0.2 mm respectively. Despite knowing the actual widths of the incident electron beams in vacuum, it was decided to keep the incident beams similar across all simulations to reduce the number of variables. It should be noted that this investigation was undertaken during the experimental phase of the research and after the main Monte Carlo simulations were run. The measured electron beam FWHM values were not used in any simulations. All simulations used an input FWHM of 2 mm.

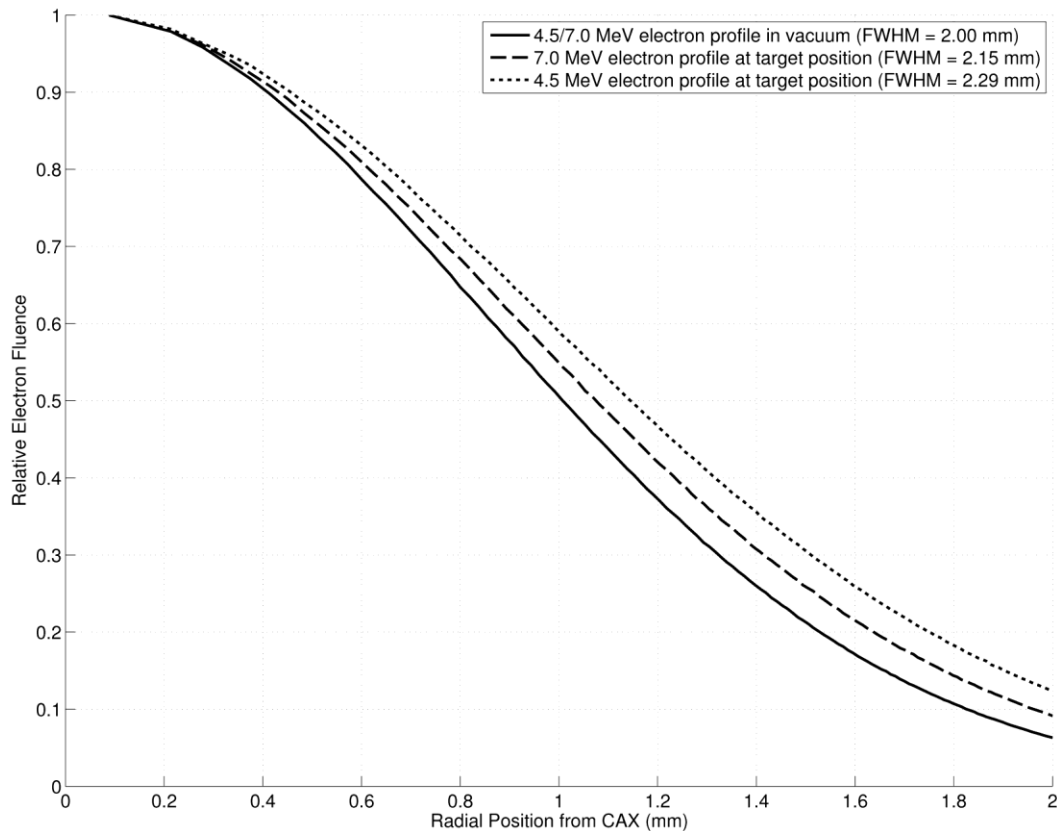


Figure 6.2: Electron fluence plotted as a function of radial position from the central axis for the 4.5 MeV and 7.0 MeV beams at the level of the external target. The electron fluence in vacuum is also shown for comparison.

6.3 Tracking the source of photons

The results summarizing the source of photon production is seen in Table 6.1. It is seen that between 2.8% (full thickness W, 7 MeV) and 10.5% (full thickness Be, 4.5 MeV) of the recorded photon fluence consisted of bremsstrahlung photons created within the exit window. This is considerably lower than the result found by Roberts *et al*² in which 70.95% of the energy fluence originated in the nickel exit window of an Elekta Ltd Precise Treatment System linac (Elekta Ltd, Crawley, UK). In the event that primary focal radiation is produced at two locations along the z axis, the acquired image will be a composite of two separate images each acquired with different magnifications. This situation is not acceptable must be

considered when using external targets placed a significant distance beyond the exit window.

Table 6.1: The percentage of photons created in different accelerator components that cross a 5 x 5 cm² plane at isocenter.

		4.5 MeV			7.0 MeV		
		Be	Al	W	Be	Al	W
10% R _{%CSDA}	Exit Window	8.3	8.2	5.4	4.3	4.7	3.5
	Target	30.7	59.7	86.7	27.9	57.0	86.4
	Jaws	5.1	3.0	0.7	4.4	3.1	0.9
	Electron filter	36.0	20.4	4.6	52.5	29.0	7.3
	Other	19.8	8.7	2.2	10.8	6.2	1.7
100% R _{%CSDA}	Exit Window	10.5	6.9	4.2	6.2	4.2	2.8
	Target	89.1	92.8	95.2	93.5	95.5	96.7
	Jaws	< 0.1	< 0.1	< 0.1	< 0.1	< 0.1	< 0.1
	Electron filter	< 0.1	< 0.1	< 0.1	< 0.1	< 0.1	< 0.1
	Other	0.4	0.3	0.2	0.3	0.2	0.2

6.4 Simulation of focal spot size for various target parameter combinations

Figure 6.3 shows the plotted results of the photon focal spot size simulation. This result was extracted from phase spaces placed at the lower surface of the

various target. Photons with angles greater than one degree off central axis were discarded to give the approximate focal spot distribution that would be observed from isocenter. Overall, the variation in HWHM is quite small between the different target combinations and there appears to be no discernable advantage to using high or low atomic number targets. As target thickness is increased there is no noticeable trend in the focal spot size. Targets exposed to the 7.0 MeV incident electron beam show no appreciable advantage over those exposed to the 4.5 MeV beam. If there are in fact any trends in photon focal spot size by varying any of the target parameters, they are obscured by the large uncertainty present in this result. It would be difficult to reduce the uncertainty much further due to the already large phase space files (4 GB for each target) and the high computational cost in analysing each phase space (one hour per target).

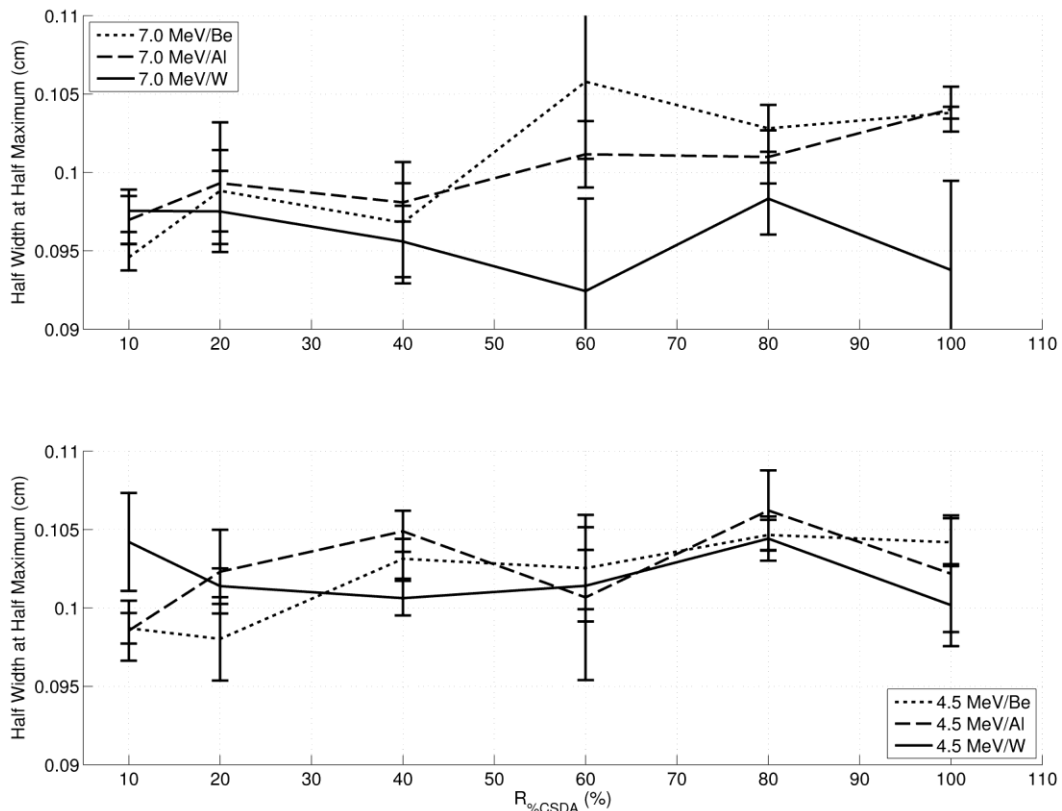


Figure 6.3: The photon focal spot half width at half maximum plotted as a function of $R_{\%CSDA}$ for various target parameters.

6.4.1 Simulation of electron beam broadening

It was hypothesised that the photon focal spot should show a clear trend of increasing FWHM as a function of increasing target thickness due to the spread of the electron beam as it travels through the target. In Figure 6.3, it was shown that this was not the case. Figure 6.4 shows the simulated electron fluence as a function of radial position from the central axis for beryllium and tungsten targets with incident 7.0 MeV electrons. Error is omitted for clarity, but is below 1% in all cases. The tungsten target shows little increase in the electron FWHM at depths of 40% and 80% of $R_{\%CSDA}$ relative to the surface of the target. However, the beryllium target shows a marked spread at greater depths. Despite high Z targets having a higher mass angular scattering power, the beryllium target has a significantly lower density (Be: 1.85, W: 19.3 cm²/g) and therefore greater physical thicknesses for a given CSDA range. For a given depth in target expressed as a percentage of the CSDA range, electrons traveled 9.68 times as far in the Z direction for the beryllium targets as for tungsten targets. The greater thickness of the beryllium target allowed broadening from electron scatter to become a significant factor in the degree of electron beam broadening. So with a clear broadening of the electron beam in low atomic number targets, one would expect to see a much broader photon focal spot in those targets as well. The fact that this trend was practically non-existent for the various targets led us to track individual photons using the latch bit to determine the depth in the target in which they were created. This is discussed in the next section.

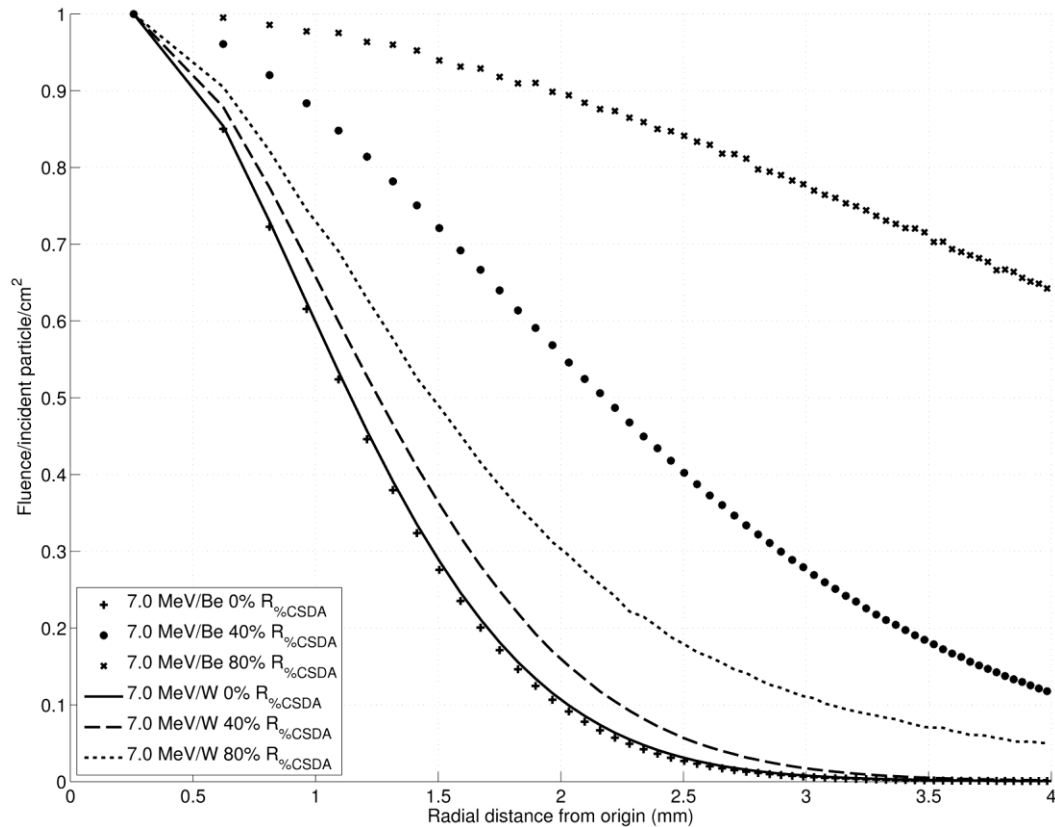


Figure 6.4: The electron fluence plotted as a function of radial position from the central axis is shown. The 7.0 MeV/Be and 7.0 MeV/W targets are shown for R_{%CSDA} values of 0%, 40% and 80%.

6.4.2 Simulation of depth of photon creation

Figure 6.5 plots the relative frequency distribution as a function of target depth. This shows that the majority of photons are created within the superficial layers of all targets. For the 4.5 MeV/Al, 7.0 MeV/Be, 7.0 MeV/Al and 7.0 MeV/W targets, 55%, 55%, 65% and 77% respectively of the photons are created at a depth less than 5% of the R_{%CSDA} value. The percentage drops off rapidly for subsequent layers and explains why thicker targets show only a marginal increase in focal spot size despite a significant broadening of the incident electron beam within the target. It is of interest to note that higher atomic number targets show a greater fraction of photons that originate in the superficial layers. Since the energy of bremsstrahlung photons is limited by the

energy of the charged particle that created it and the mean electron energy decreases as a function of depth in the target, it follows that the mean photon energy also decreases as a function of depth. Due to the Z^3 dependence of the mass photoelectric attenuation coefficient, it is reasonable to conclude that the higher atomic number targets reabsorb many of the relatively lower energy photons created in the deeper layers and the photons scored in the phase space consist mostly of the relatively higher energy photons created within the superficial layers.

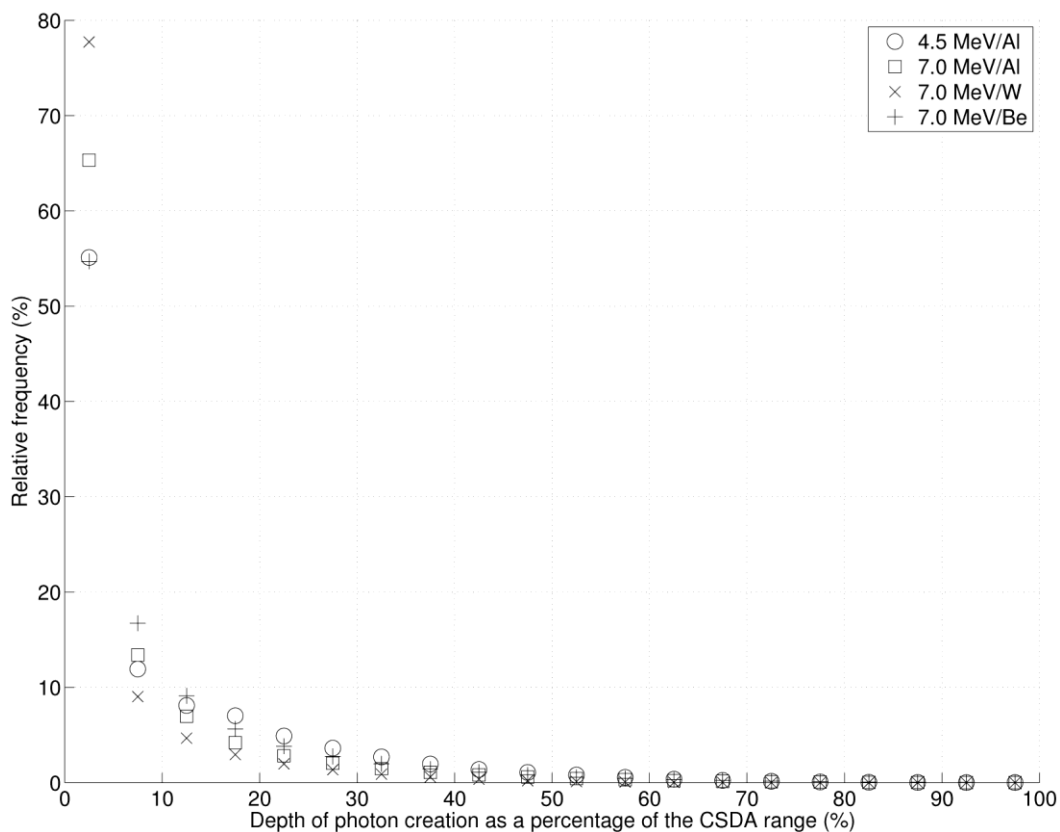


Figure 6.5: A relative frequency distribution of the depth in target of photon creation for the 4.5 MeV/Al, 7.0 MeV/Al, 7.0 MeV/W and 7.0 MeV/Be targets.

6.5 Simulated photon fluence from a modeled line pair phantom

Figure 6.6 shows the calculated f_{50} values plotted against $R_{\%CSDA}$ for all simulated target parameter combinations. It can be seen that there is a small advantage in using thin targets over full thickness targets. As discussed in section 6.4.1, there

is a moderate widening of the incident electron beam at greater depths in the target due to scatter. It follows then that the bremsstrahlung photon distribution created at increasing depths will have a wider FWHM. By using a relatively thin target, the photons that would have been created from the relatively broad distribution at greater depths are eliminated, resulting in a smaller focal spot. Although the photon focal spot size was investigated in section 0 for different target parameters, the uncertainty was too great to make any comparison to the simulated f_{50} results.

For a given $R_{\%CSDA}$, higher atomic number targets show higher f_{50} values, particularly for target thicknesses greater than 60% of the CSDA range. In section 6.4.1, it was shown that the electron beam FWHM in a beryllium target increased more rapidly than that of a tungsten target as a function of $R_{\%CSDA}$. It follows then that the low Z targets would also have relatively larger photon focal spots when compared to higher Z targets.

Targets with 7 MeV incident electrons showed superior results to those with 4.5 MeV incident electrons. In section 6.2, it was shown that the 4.5 MeV electron beam broadened more after passing through the exit window and air gap than the 7.0 MeV beam due to the higher mass angular scattering power of lower energy electrons. Since the incident FWHM value was set to 2 mm for all simulations, the 4.5 MeV targets would have been exposed to a broader incident electron beam which would also result in a wider focal spot. As the MTF is quite sensitive to focal spot size, it stands to reason that the f_{50} values of the 7.0 MeV beams would be greater than the 4.5 MeV beams. The contribution to the resolution degradation from electron scatter in the beryllium window and in air could be eliminated by placing the external target in vacuum at the position of the therapy target. This solution is discussed below in section 6.7. The simulated clinical 6 MV beam is included in the figure for comparison. Due to the geometric advantage of being placed further away from the phantom and imager, as well as being located within the vacuum system where electron scatter in the air and

beryllium window is eliminated, it shows a substantial advantage over the external targets.

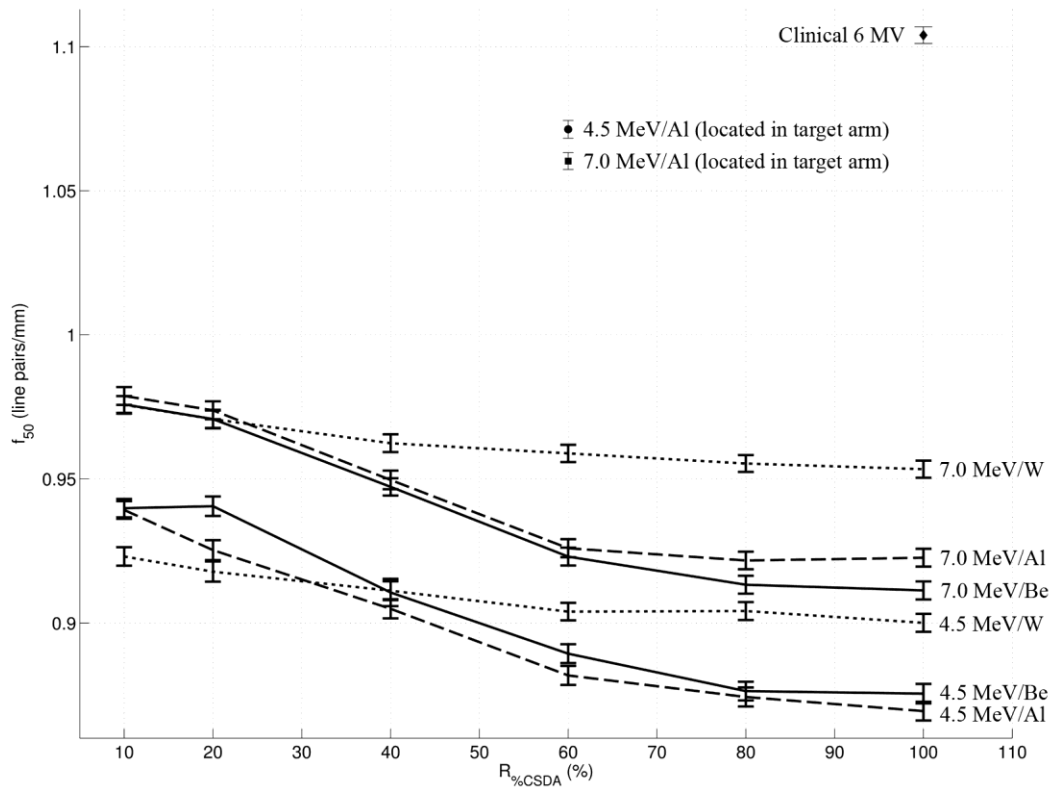


Figure 6.6: Simulated f_{50} values as a function of $R_{\%CSDA}$ for various target parameters. Included for comparison are the f_{50} values for the 4.5 MeV/Al and 7.0 MeV/Al targets at the location of the clinical target arm as well as the clinical 6 MV beam.

6.6 Experimental determination of f_{50} .

Figure 6.7 shows three images of the QC3 phantom acquired by different targets. All images had the black and white levels set to the 1.5 cm PVC and 1.5 cm lead contrast regions of the QC3 respectively. Figure 6.7 (a) was taken using the clinical 6 MV beam line and is compared to the best (Figure 6.7 (b); 7.0 MeV/Be, 20% $R_{\%CSDA}$) and worst case (Figure 6.7 (c); 4.5 MeV/W, 100% $R_{\%CSDA}$) targets.

The calculated f_{50} values as a function of target thickness are seen in Figure 6.8. Note that the overall f_{50} values are lower compared to the simulated values due

to the detector's contribution to the total MTF. The trend of decreasing f_{50} with target thickness is again observed in the experimental results.

The experimental results show a reversal in the trend of higher f_{50} values for higher Z materials that was observed in the simulated results found in Figure 6.6. Munro and Bouius³ reported a line spread function (LSF) dependence on the nominal beam energy when using an amorphous silicon based EPID. It was demonstrated that an 18 MV beam produced a broader LSF when compared to a 6 MV beam, apparently resulting from the increased lateral migration of higher energy electrons within the copper layer/phosphor screen for the former, which causes a broadening of the central region of the LSF.

Typical photon spectra produced by low Z targets contain a much higher fraction of photons in the diagnostic energy range and hence a lower mean energy. This is illustrated in Figure 6.9 which shows the relative photon fluence as a function of energy. Spectra were extracted from a 10 cm diameter circular region in the various phase spaces analysed in section 6.5. Each curve was normalized to its total area. With reference to Munro's result, this would imply that imaging using low Z targets would cause the detector to exhibit a sharper LSF than harder spectra produced by higher atomic number targets. This effect appears to be the dominant factor in determining which target materials are superior from a spatial resolution standpoint when using EPID devices and explains the reversal in trend from the simulated results.

Targets with 7.0 MeV incident electrons are superior to their 4.5 MeV counterparts in terms of f_{50} . As discussed in section 6.2, the electron beam was found to broaden more for lower energy electrons due to their higher mass angular scattering power. It follows then that the targets with incident 4.5 MeV electrons will have a wider FWHM at a given $R_{\%CSDA}$ and thus have a wider focal spot. Spatial resolution is very sensitive to increases in the focal spot size and this effect dominates over any advantage due to the detectors favourable LSF for lower photon energies.

Figure 6.8 also shows the measured f_{50} value calculated from the clinical 6 MV beam. Experimental f_{50} values ranged between 10.4% below (4.5 MeV/W) and 15.5% above (7.0 MeV/Be) the 6 MV value. It is interesting to note that despite the 6 MV target being located within vacuum, where electron beam spread is eliminated, and having a geometric advantage due to its greater distance from the phantom and imager, it shows no appreciable advantage over many of the external target combinations. It is likely that the clinical beam would show improvement in f_{50} if the flattening filter were removed from the beamline. This would result in less beam hardening and allow the image to benefit from the detector's superior LSF for lower photon beam quality. As it stands, the advantages of the target being located in vacuum and having a greater distance from the object and imager appear to be offset to some degree by the detector's MTF dependence on photon energy. One other factor that can cause resolution degradation was discussed by Faddegon *et al*⁴. They highlighted that the flattening filter present in the 6 MV clinical beam line is a major source of extra focal radiation that can have an adverse effect on the MTF.

It should be noted that targets placed in the target arm will show an increased degradation in the detector component of the total MTF due to the imager's finite pixel size and pixel number (the object will be projected onto a smaller area). Whether the total MTF will improve or degrade will depend upon the size of the focal spot and the pixel density of the detector.

Overall, the results presented here indicate that from a spatial resolution standpoint, there is no considerable disadvantage in using low Z targets external targets over the clinical beam, in fact there is a small improvement in spatial resolution for some target/energy combinations in addition to the appreciable contrast gains (contrast improvement factor increase of 2-3) reported on by other authors⁵.

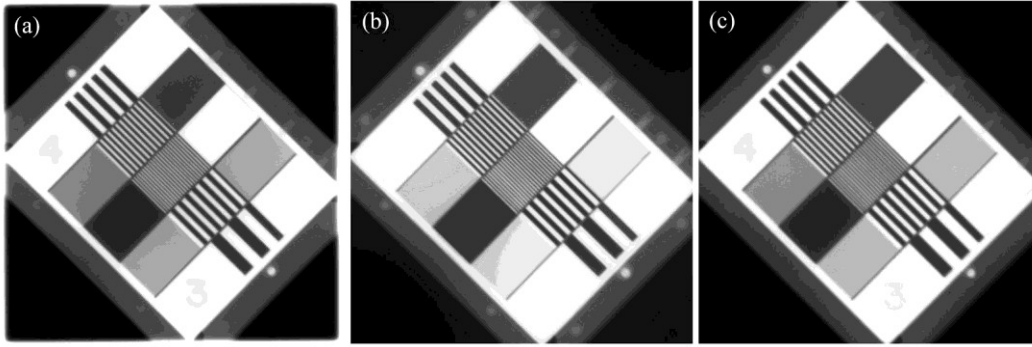


Figure 6.7: (a) A planar image of the QC3 taken with the clinical 6 MV beam. (b) The 20% thickness Be target with 7.0 MeV incident electrons which gave the highest f_{50} value. (c) The 100% thickness W target with 4.5 MeV incident electrons which gave the lowest f_{50} value.

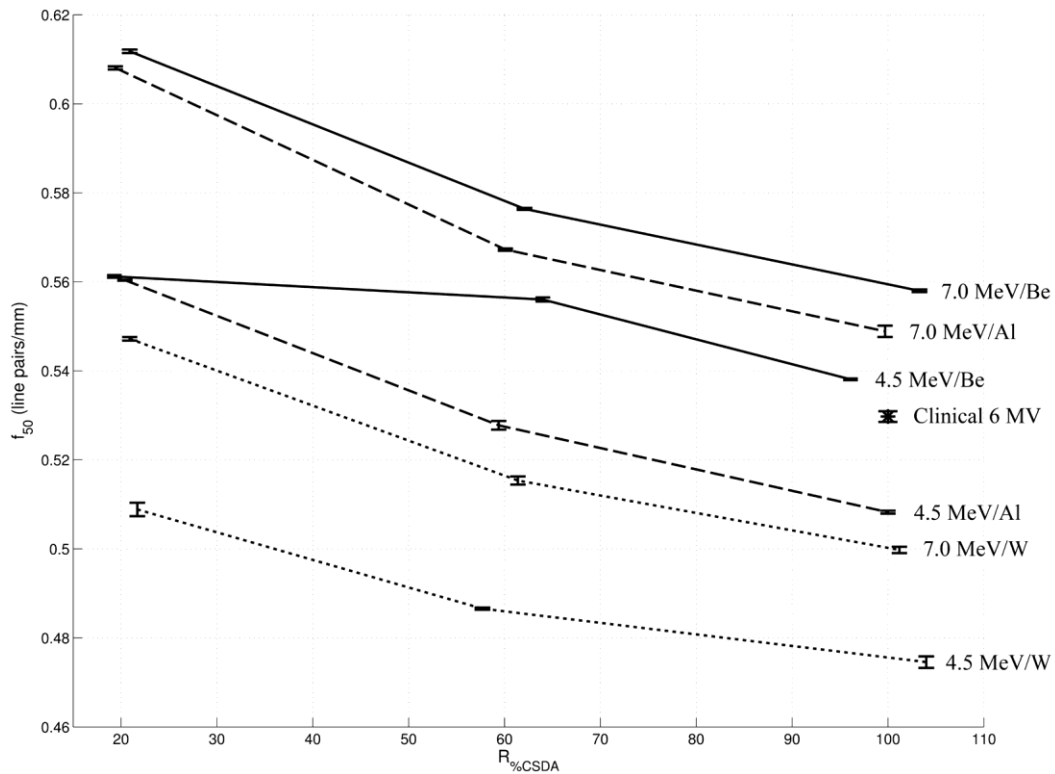


Figure 6.8: Experimental f_{50} values for all target combinations as a function of target thickness as a percentage of R_{CSDA} . The f_{50} value from the clinical 6 MV beam is also included for comparison.

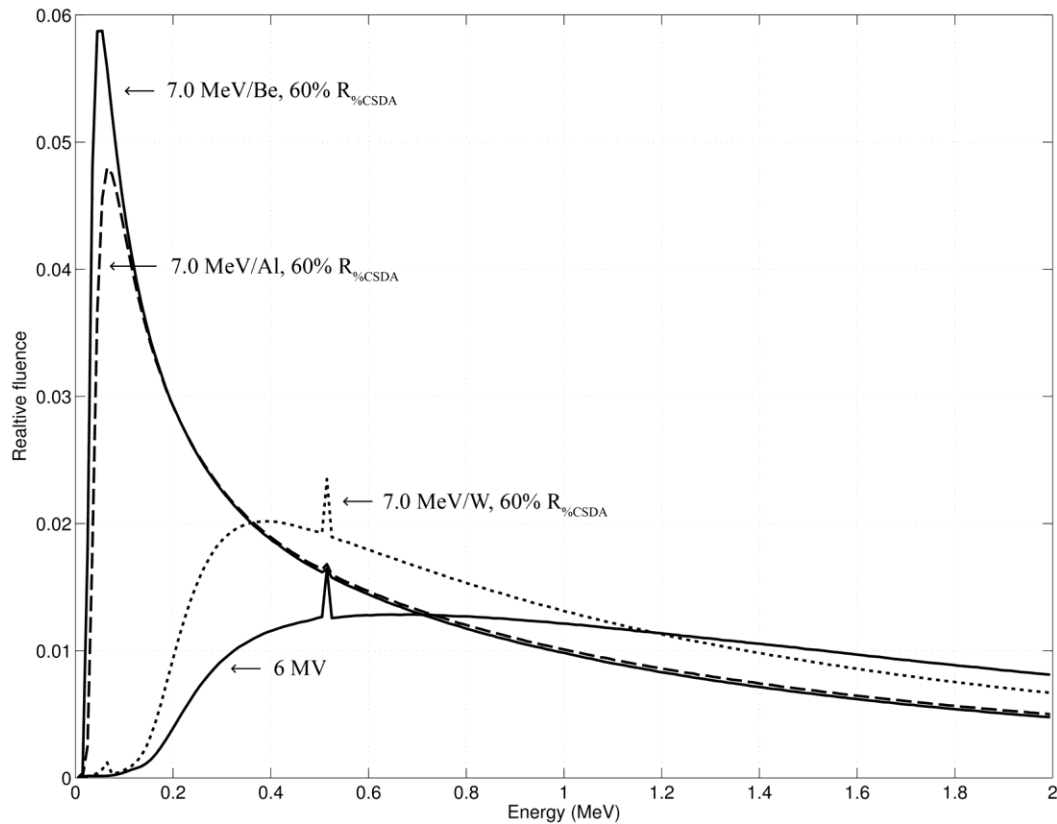


Figure 6.9: Monte Carlo generated relative fluence energy spectra for three custom targets, compared to the clinical 6 MV beam. Each curve is normalized by its area.

6.7 Resolution improvement in moving the low-Z target into the target arm

Spatial resolution is highly dependent upon the x-ray focal spot size. Due to the transmission of incident electrons through the beryllium exit window and 9 mm of air, a broadening of the electron beam FWHM was calculated in section 6.2 to be 13.8% and 6.7% for 4.5 and 7.0 MeV incident electrons, respectively, when compared to the FWHM above the Be exit window. By moving the target into the target arm, the issue of electron beam broadening due to scatter is avoided. Simulations were run with 60% aluminum targets placed at the location of the clinical target for both incident electron energies. Calculated f_{50} values were found to be 14.5% and 21.5% higher for the 7.0 MeV and 4.5 MeV targets respectively. As expected, positioning the target within the vacuum system led

to an improvement in spatial resolution and was the single most influential parameter when compared to the choice of target energy, material and thickness. However, in all cases, spatial resolution proved to be quite acceptable when compared to the clinical 6 MV beam and the use of external targets appears to be feasible provided that an effort is made to minimize the distance between the target and the exit window. Due to the location of the external targets, beam divergence will no longer be matched to the jaw edges; however, this should not be an issue due to the fact that sharp penumbra regions are not necessary for imaging. Also, any change in magnification due to new imaging geometry could be accounted for by software.

6.8 Spatial resolution assessment in cone-beam CT

Reconstructed axial slices from volumetric CBCT image sets from the three imaging modes are shown in Figure 6.10 (a), (b) and (c). The highest spatial frequency that could be identified for the 6 MV imaging mode was 0.4 line pairs/mm. For both the 3.5 MeV/Al and 7.0 MeV/Al modes, the highest visible spatial frequency was 0.5 line pairs/mm. These results are consistent with those found by Faddegon *et al*⁴ who reported higher spatial resolution in CBCT using unflattened beams from a carbon target installed in a Siemens Primus linac (Siemens Medical, Erlangen, Germany), when compared to the treatment beam. Using the imaging beamline, they were able to visually distinguish the 0.4 lp/mm region as compared to 0.2 lp/mm when the treatment beamline was used. Included as a comparison in Figure 6.10 (d) is a slice from a cone-beam acquisition from the same phantom acquired using an Acuity simulator (Varian Medical Inc.) set to 125 kVp. In this image it is possible to visually distinguish up to 1.0 lp/mm. Kamath *et al*⁶ made a comparison between kilovoltage imaging systems with the CatPhan (The Phantom Laboratory Inc.). They found that the Varian On-Board Imager (Varian Medical Systems) was able to resolve 1 lp/mm

while the Elekta X-ray Volumetric Imager (Elekta Medical Systems) was able to resolve 0.2 lp/mm.

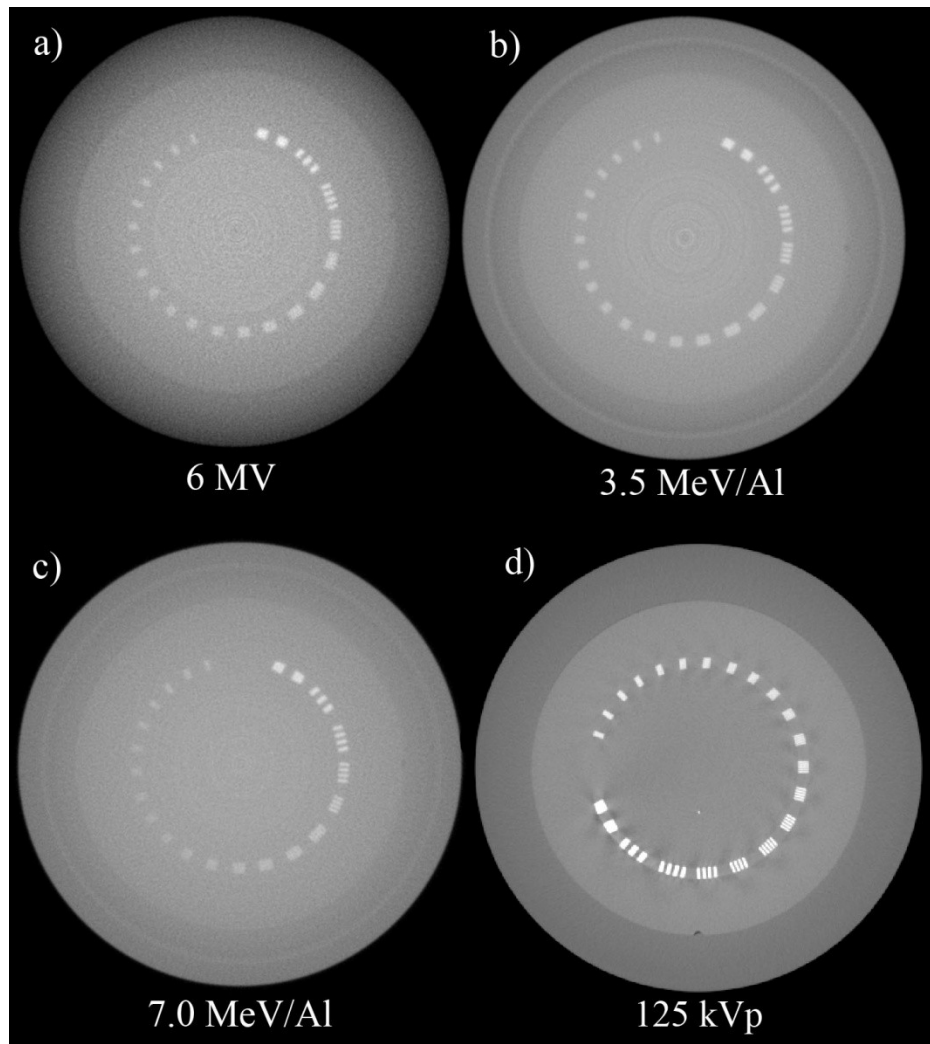


Figure 6.10: MV CBCT axial slices of the spatial resolution section of the Catphan phantom acquired with the (a) 6 MV, (b) the 3.5 MeV/Al and the (c) 7.0 MeV/Al beams. (d) A cone beam set acquired of the same phantom using a 125 kVp conventional simulator.

6.9 Clinical implementation of a low-Z, external target imaging mode

The main motivation for the implementation of a low-Z, external-target imaging mode is the increase in contrast to noise ratio, although, there are many factors

that must be considered before this method can be implemented clinically. This work was meant to systematically investigate whether the approach was viable from a spatial resolution point of view.

The implementation of a low-Z-target imaging system proves to be quite feasible due to the limited amount of modifications required to the accelerator. To make this setup practical for clinical use, the electron filter could be moved up into the carousel below the target or full thickness low-Z targets could be used. This would eliminate the need for insertion and removal of the filter when switching between the treatment and imaging modes. The act of switching modes would be done in the same manner as selecting different photon energies. A short three to five second delay would be involved in switching modes due to the time required to reposition the carousel, however, this would still be acceptable for intra-fractional imaging.

Currently, images are acquired with the accelerator operating in electron mode. This leads to relatively long exposure times (dependent upon target choice) due to the reduced beam current of about two orders of magnitude compared to photon modes. It would be advantageous to insert a separate program board that would effectively operate in electron mode, but allow the higher beam currents used in the photon modes. By using its own program board, new normal operating conditions could be established that would remove the requirement to override the dosimetric interlocks and enable the use of the beam monitoring system that is required from a safety standpoint to ensure that excess dose is not received by the patient. The issue of target cooling, which is an important consideration for targets located in vacuum, is not a concern for externally mounted targets as they are exposed to open atmosphere. Low-Z targets have the advantage of producing softer beams which show increased differential attenuation between different absorber media which in turn leads to increased contrast. Also, softer beams have the advantage of higher detection efficiency due to their high interaction probability leading to lower noise for a

given patient dose. It is expected then that the imaging dose to the patient from a low-Z imaging beam should give a relatively lower patient dose for a given contrast to noise ratio when compared to the currently used 6 MV portal imaging systems.

6.10 References

1. D. A. Jaffray, J. J. Battista, A. Fenster and P. Munro, "X-ray sources of medical linear accelerators: Focal and extra-focal radiation," *Med. Phys.* **20**, 1417-1427 (1993).
2. D. A. Roberts, V. N. Hansen, A. C. Niven, M. G. Thompson, J. Seco and P. M. Evans, "A low Z linac and flat panel imager: comparison with the conventional imaging approach," *Phys. Med. Biol.* **53**, 6305-6319 (2008).
3. P. Munro and D. C. Bouius, "X-ray quantum limited portal imaging using amorphous silicon flat-panel arrays," *Med. Phys.* **25**, 689-702 (1997).
4. B. A. Faddegon, V. Wu and J. Pouliot, "Low dose megavoltage cone beam computed tomography with and unflattened 4 MV beam from a carbon target," *Med. Phys.* **35**, 5777-5786 (2008).
5. E. J. Orton and J. L. Robar, "Megavoltage image contrast with low-atomic number target materials and amorphous silicon electric portal imagers," *Phys. Med. Biol.* **54**, 1275-1289 (2009).
6. S. Kamath, W. Song, A. Chvetsov, J. Li, S. Ozawa, C. Liu and J. Palta, presented at the AAPM Annual Meeting, 2008 (unpublished).

Chapter 7

CONCLUSIONS

7.1 SUMMARY	78
7.2 FUTURE WORK.....	79

7.1 Summary

Monte Carlo and experimental investigations with low-Z external targets were carried out on a Varian linear accelerator and showed that by minimizing the separation between the exit window and the target, reasonably sharp images that are on par or better than those acquired with the clinical 6 MV beam can be achieved. Simulated and experimental results show that thinner targets are generally superior to thicker targets and that higher incident electron energies produce better results. Simulated results showed that higher Z materials gave higher f_{50} values, however, with the introduction of the aS1000 imager in the experimental investigation the trend was reversed to show that lower Z targets produced superior results due to the imagers MTF dependence on energy. It is hypothesized that by placing the external low-Z targets within the vacuum system alongside the clinical target, further improvements in spatial resolution can be realized that surpass those of current on-board MV imaging systems.

Simulations showed a 14.5% and 21.5% increase in f_{50} for the 7.0 MeV and 4.5 MeV targets respectively when moved from the carousel to the location of the clinical target. The f_{50} value of the custom targets were compared to the clinical 6 MV beam and were found to be between 10.4% lower and 15.5% higher than the 6 MV value.

Cone-beam sets acquired with a low-Z target showed superior spatial resolution values when compared to sets acquired with the clinical 6 MV beam. Low-Z sets

were compared to a kilovoltage cone-beam acquisition and it was found that the kilovoltage set showed significantly higher spatial resolution.

The findings of this work along with the previously investigated work on contrast by other authors show that low Z external targets can provide a significant overall improvement in image quality and would be clinically advantageous in MV portal imaging and CBCT applications.

7.2 Future Work

This work has shown the initial results of the feasibility of externally placed, low-Z targets from a spatial resolution point of view. Further work is required before this concept can be applied in a clinical setting. Further investigation into increasing the beam current to improve photon fluence and shorten exposure times is required as well as integrating the electron filter into the carousel.

As the spatial resolution in the planar imaging was characterized using relative MTF curves, it would be beneficial to extract an absolute MTF curve using a line spread function to make a comparison with other planar imaging systems.

The 1 mm copper build up layer in the aS1000 imager was optimized by the manufacturer for use in hardened 6 MV beams. With the changes in the energy spectrum from the use of low-Z targets in the absence of a flattening filter, many of the useful photons in the diagnostic energy range will produce secondary particles with insufficient kinetic energy to reach the scintillator, effectively removing their contribution to the image. This would have an effect on contrast as well as spatial resolution due to increased lateral migration of secondary particles in the buildup layer. It would be of interest to optimize the thickness of this copper layer.

Bibliography

1. E. J. Orton and J. L. Robar, "Megavoltage image contrast with low-atomic number target materials and amorphous silicon electric portal imagers," *Phys. Med. Biol.* **54**, 1275-1289 (2009).
2. K. Knight, N. Touma, L. Zhu, G. Duchesne and J. Cox, "Implementation of daily image-guided radiation therapy using an in-room CT scanner for prostate cancer isocenter localization," *J Med Imaging Radiat Oncol* **53**, 132-138 (2009).
3. J. Lagendijk, B. Raatmakers, A. Raaijmakers, J. Overweg, K. Brown, E. Kerkhof, R. van der Put, B. Hardmark, M. van Vulpen and U. van der Heide, "MRI/linac integration," *Radiother Oncol* **86**, 25-29 (2008).
4. D. A. Jaffray, J. H. Siewerdsen, J. W. Wong and A. A. Martinez, "Flat-panel cone-beam computed tomography for image guided radiation therapy," *Int. J. Radiation Oncology Biol. Phys.* **53**, 1337-1349 (2002).
5. A. Sarfehnia, K. Jabbari, J. Seuntjens and E. B. Podgorsak, "Experimental verification of beam quality in high-contrast imaging with orthogonal bremsstrahlung photon beams," *Med. Phys.* **34**, 2896-2906 (2007).
6. D. M. Galbraith, "Low-energy imaging with high-energy bremsstrahlung beams," *Med. Phys.* **16**, 734-746 (1989).
7. A. Tsechanski, A. F. Bielajew, S. Faermann and Y. Krutmann, "A thin target approach for portal imaging in medical accelerators," *Phys. Med. Biol.* **43**, 2221-2236 (1998).
8. O. Z. Ostapiak, P. F. O'Brien and B. A. Faddegon, "Megavoltage imaging with low Z targets: implementation and characterization of an investigational system," *Med. Phys.* **25**, 1910-1918 (1998).
9. S. Flampouri, P. M. Evans, F. Verhaegen, A. E. Nahum, E. Spezi and M. Partridge, "Optimization of accelerator target and detector for portal imaging using Monte Carlo simulation and experiment," *Phys. Med. Biol.* **47**, 3331-3349 (2002).
10. D. A. Roberts, V. N. Hansen, A. C. Niven, M. G. Thompson, J. Seco and P. M. Evans, "A low Z linac and flat panel imager: comparison with the conventional imaging approach," *Phys. Med. Biol.* **53**, 6305-6319 (2008).
11. ICRU, "Stopping powers for electrons and positrons," ICRU Report 37 (1984).
12. E. B. Podgorsak, *Radiation Physics for Medical Physicists*. (Springer, 2006).

13. E. B. Podgorsak, *Radiation Oncology Physics: A Handbook for Teachers and Students*. (IAEA, 2005).
14. J. Cygler, G. Daskalov, G. Chan and G. Ding, "Evaluation of the first commercial Monte Carlo dose calculation engine for electron beam treatment planning," *Med. Phys.* **31**, 142-153 (2004).
15. E. Heath and J. Seuntjens, "Dosimetric evaluation of the clinical implementation of the first commercial IMRT Monte Carlo treatment planning system at 6 MV," *Med. Phys.* **31**, 2771-2779 (2004).
16. D. W. O. Rogers, "Fifty years of Monte Carlo simulations for medical physics," *Phys Med Biol* **51**, R287-301 (2006).
17. D. W. O. Rogers, B. A. Faddegon, G. X. Ding, C. M. Ma, J. We and T. R. Mackie, "BEAM: a Monte Carlo code to simulate radiotherapy treatment units," *Med. Phys.* **22**, 503-524 (1995).
18. D. W. O. Rogers, B. Walters and I. Kawrakow, Report No. PIRS-0509(A)revK, 2006.
19. R. Rajapakshe, T. J. Radcliffe and S. Shalev, "Quality control for on-line portal imaging systems," *Proc. SPIE* **1897**, 121-127 (1993).
20. R. Rajapakshe, K. Luchka and S. Shalev, "A quality control test for electronic portal imaging devices," *Med. Phys.* **23**, 1237-1244 (1996).
21. J. Coltman, "The Specification of Imaging Properties by Response to a Sine Wave Input," *J. Opt. Soc. Am.* **44**, 468-469 (1954).
22. R. T. Droege and R. L. Morin, "A practical method to measure the MTF of CT scanners," *Med. Phys.* **9**, 758-760 (1982).
23. C. Karzmark, C. Nunan and E. Tanabe, *Medical Electron Accelerators*. (McGraw-Hill, 1992).
24. J. L. Robar, "Generation and modeling of megavoltage photon beams for contrast-enhanced radiation therapy," *Phys. Med. Biol.* **51**, 5487-5504 (2006).
25. C. M. Ma and D. W. O. Rogers, Report No. PIRS-0509(C)revA, 2007.
26. D. A. Jaffray, J. J. Battista, A. Fenster and P. Munro, "X-ray sources of medical linear accelerators: Focal and extra-focal radiation," *Med. Phys.* **20**, 1417-1427 (1993).
27. B. A. Faddegon, V. Wu and J. Pouliot, "Low dose megavoltage cone beam computed tomography with and unflattened 4 MV beam from a carbon target," *Med. Phys.* **35**, 5777-5786 (2008).
28. J. L. Robar, T. Connell, W. Huang and R. Kelly, "Megavoltage planar and cone-beam imaging with aluminum linear accelerator targets:

dependence of image quality improvement on beam energy and patient separation," (2009).

29. L. A. Feldkemp, L. C. Davis and J. W. Kress, "Practicle cone-beam algorithm," J. Opt. Soc. Am. **1**, 612-619 (1984).
30. P. Munro and D. C. Bouius, "X-ray quantum limited portal imaging using amorphous silicon flat-panel arrays," Med. Phys. **25**, 689-702 (1997).
31. S. Kamath, W. Song, A. Chvetsov, J. Li, S. Ozawa, C. Liu and J. Palta, presented at the AAPM Annual Meeting, 2008 (unpublished).

Appendix A IAS3 parameters

BeamOnDelay	63	Init	Yes
TriggerDelay	6	SourceSelect	HOTLink
LineStartDelay	2	XRayGenTrig	Yes
LinePerSync	5	AddMachineData	Yes
BeamPulsePerFrame	9	TestImageDataWidth	14 bits
XRayCycleTime	6	TestImageOn	No
XRayPulseWidth1	1	TestImageMode	Z = 16 * X + 16 * Y
XRayPulseWidth2	20	Machine	Clinac Research
HOTLinkReframe	Yes	FrameProcessingF	LVDS
HOTLinkAllowCommand	No	TimeTagRecording	Yes
HOTLinkBISTEN	No	XRayDisable	No
BISTError	0	Config_11	No
BridgeControl	0	DoubleXRayPulse	No
BridgeTXLength	0	EdgePulse	No
DACData	0	PFS	No
CTEnable	No	IntegratedAcquisition	No
CTReserved1	No	Acquire	Yes
CTReserved2	No	FrameStartSignal	XRayGenTrig
CTCalibrateADC	No	EdgeSense	Rising Edge
CTNormChamberGain	5.1 Hz	SyncType	Synchronized to Machine Trigger Signals
CTAngleIncrements	0	SyncMode	Synchronized to Machine Sync Signal
CTPresetGantryAngle	0.000000	AcqConfig_9	No
BeamOff	No	AutoBeamOff	No
DRSFreeze	No	BeamOnDelayEnable	Yes
SNIL	Yes	RadShot	No
BeamHold	No	ContinuousWave	No
SpareLS1	No	GatedBeamControl	No
SpareHS1	No	EventSelect	Beam Pulses
SigOut_6	No	IDUClockValidDelay	10
SigOut_7	No	NoOffFrame	10
CTScanAngleLowerLimit	0.000000	NoOfResetFrame	1
CTScanAngleUpperLimit	0.000000	FrameStartDelay	0

Appendix B Main BEAMnrc input file

```
Al6_Sp
#!GUI1.0
5 AIR700ICRU
0, 0, 0, 0, 1, 3, 0, IWATCH ETC.
1000, 20, 40, 1000, 2, 1000, 0, 0, NCASE ETC.
20, 100, 7, 2, 1, 58.5, DIRECTIONAL BREM OPTIONS
-1, 19, -0.2, 0, 0, 0, 0.0, 0.0, 0.0, 0.0, IQIN, ISOURCE + OPTIONS
10 0, MONOENERGETIC
7
0, 0, 0.7, 0.01, 0, 0, , 0 , ECUT, PCUT, IREJCT, ESAVE
0, 0, 0, 0, 0, PHOTON FORCING
1, 11, SCORING INPUT
15 1, 1
5.2,
0, DOSE COMPONENTS
0.0, Z TO FRONT FACE
***** start of CM FLATFILT with identifier pricol *****
20 5, RMAX
PrimaryCollimation
0, ZMIN
5, NUMBER OF LAYERS
1, 1.6, # CONES, ZTHICK OF LAYER 1
25 4.6,
4.6,
1, 6, # CONES, ZTHICK OF LAYER 2
0.398925,
1.894893,
30 1, 1.4, # CONES, ZTHICK OF LAYER 3
4.9,
4.9,
1, 0.0254, # CONES, ZTHICK OF LAYER 4
4.9,
35 4.9,
1, 0.89559, # CONES, ZTHICK OF LAYER 5
4.99,
4.99,
0, 0, 0, 0,
40 VACUUM
0, 0, 0, 2,
W700ICRU
0, 0, 0, 0,
VACUUM
45 0, 0, 0, 0,
W700ICRU
0, 0, 0, 0,
VACUUM
0, 0, 0, 0,
50 VACUUM
0, 0, 0, 3,
BE700ICRU
0, 0, 0, 3,
BE700ICRU
55 0.7, 0.01, 0, 0,
AIR700ICRU
0.7, 0.01, 0, 0,
AL700ICRU
***** start of CM FLATFILT with identifier lowztarg *****
60 5, RMAX
LowZ - Al High
```

```

9.971, ZMIN
1, NUMBER OF LAYERS
1, 1.57, # CONES, ZTHICK OF LAYER 1
65 4.99,
4.99,
0, 0, 0, 4,
AL700ICRU
0, 0, 0, 0,
70 AIR700ICRU
***** start of CM SLABS with identifier chamber *****
5, RMAX
IonChamber
15, NSLABS
75 14.2, ZMIN
0.629, 0, 0, 0, 0, 0
AIR700ICRU
0.013, 0, 0, 0, 5, 0
KAPTON700ICRU
80 0.229, 0, 0, 0, 0, 0
AIR700ICRU
0.005, 0, 0, 0, 5, 0
KAPTON700ICRU
0.234, 0, 0, 0, 0, 0
85 AIR700ICRU
0.005, 0, 0, 0, 5, 0
KAPTON700ICRU
0.229, 0, 0, 0, 0, 0
AIR700ICRU
90 0.013, 0, 0, 0, 5, 0
KAPTON700ICRU
0.229, 0, 0, 0, 0, 0
AIR700ICRU
0.005, 0, 0, 0, 5, 0
95 KAPTON700ICRU
0.234, 0, 0, 0, 0, 0
AIR700ICRU
0.005, 0, 0, 0, 5, 0
KAPTON700ICRU
100 0.229, 0, 0, 0, 0, 0
AIR700ICRU
0.013, 0, 0, 0, 5, 0
KAPTON700ICRU
0.629, 0, 0, 0, 0, 0
105 AIR700ICRU
***** start of CM MIRROR with identifier mirror *****
7.1452, RMAX
Mirror
18.5, 8.5, ZMIN, ZTHICK
110 4.9941, -7.1452, XFMIN, XBMIN
1, # LAYERS
0.0088567, thickness of layer 1
0, 0, 0, 6,
MYLAR700ICRU
115 0, 0, 0, 0,
AIR700ICRU
0, 0, 0, 0,
AIR700ICRU
***** start of CM JAWS with identifier jaws *****
120 11.5, RMAX
Secondary Collimation
2, # PAIRED BARS OR JAWS
Y
28, 35.8, 2.24, 2.864, -2.24, -2.864,

```

```

125 X
    36.7, 44.5, 2.936, 3.56, -2.936, -3.56,
    0, 0, 0, 0,
    0, 0, 0, 7,
    W700ICRU
130 0, 0, 0, 7,
    W700ICRU
    ***** start of CM SLABS with identifier mylarsty *****
    14.3, RMAX
    Mylar & Polysty filter
135 2, NSLABS
    57.3, ZMIN
    0.01016, 0, 0, 0, 8, 0
    MYLAR700ICRU
    0.5, 0, 0, 0, 0, 0
140 AIR700ICRU
    ***** start of CM FLATFILT with identifier poly *****
    11.5, RMAX
    LowZ - Al High
    57.81016, ZMIN
145 1, NUMBER OF LAYERS
    1, 3.29, # CONES, ZTHICK OF LAYER 1
    14.3,
    14.3,
    0, 0, 0, 0,
150 POLYSTY700ICRU
    0, 0, 0, 0,
    AIR700ICRU
    ***** start of CM SLABS with identifier frcov *****
    4.2, RMAX
    Front Cover QC3
155 1, NSLABS
    99.06, ZMIN
    0.3, 0, 0, 0, 0, 0
    PMMA700ICRU
160 ***** start of CM VARMLC with identifier spphant *****
    4.2, RMAX
    Spatial Phantom QC3
    1, 5, ORIENT, NGROUP
    99.3601, ZMIN
165 1.4999, ZTHICK
    4, 0.25
    6, 0.0667
    10, 0.0427
    8, 0.05
170 5, 0.125
    -1.4, START
    0, 0, WSCREW, HSCREW
    0, 0, 0, WTONGUE, HTONGUE, ZTONGUE
    0, 0, 0, WGROOVE, HGROOVE, ZGROOVE
175 0, LEAFGAP
    1, ENDTYPE
    -99999, ZFOCUS or RADIUS of leaf ends
    9.921, ZFOCUS of leaf sides
    0, 0, 1
180 -4, 4, 1
    0, 0, 1
    -4, 4, 1
    0, 0, 1
    -4, 4, 1
185 0, 0, 1
    -4, 4, 1
    0, 0, 1

```

```

-4, 4, 1
0, 0, 1
190 -4, 4, 1
0, 0, 1
-4, 4, 1
0, 0, 1
-4, 4, 1
195 0, 0, 1
-4, 4, 1
0, 0, 1
-4, 4, 1
0, 0, 1
200 -4, 4, 1
0, 0, 1
-4, 4, 1
0, 0, 1
-4, 4, 1
205 0, 0, 1
-4, 4, 1
0, 0, 1
-4, 4, 1
0, 0, 1
210 -4, 4, 1
0, 0, 1
0, 0, 0, 10,
delrin700
0, 0, 0, 11, 0,
215 PB700ICRU
***** start of CM SLABS with identifier bkcov *****
4.5, RMAX
Back Cover
2, NSLABS
220 100.86, ZMIN
0.2, 0, 0, 0, 0, 0
AL700ICRU
1.79, 0, 0, 0, 0, 0
PMMA700ICRU
225 ***** start of CM SLABS with identifier airgap *****
5, RMAX
Air Gap
1, NSLABS
102.85, ZMIN
230 27.15, 0.7, 0.01, 0, 0, 0
AIR700ICRU
*****end of all CMs*****
#####
:Start MC Transport Parameter:
235
Global ECUT= 0.7
Global PCUT= 0.01
Global SMAX= 5
ESTEPE= 0.25
240 XIMAX= 0.5
Boundary crossing algorithm= EXACT
Skin depth for BCA= 0
Electron-step algorithm= PRESTA-II
Spin effects= On
245 Brems angular sampling= Simple
Brems cross sections= BH
Bound Compton scattering= Off
Pair angular sampling= Simple
Photoelectron angular sampling= Off
250 Rayleigh scattering= Off

```

Atomic relaxations= Off
Electron impact ionization= Off

255 :Stop MC Transport Parameter:
#####